frontiers in Earth Science

ORIGINAL RESEARCH
published: 25 October 2019
doi: 10.3389/feart.2019.00271

Rapid Magma Generation or Shared Magmatic Reservoir? Petrology and Geochronology of the Rat Creek and Nelson Mountain Tuffs, CO, USA

Jakub Sliwinski[1], David Farsky[1], Peter W. Lipman[2], Marcel Guillong[1] and Olivier Bachmann[1]*

[1] *Institute of Geochemistry and Petrology, ETH Zürich, Zurich, Switzerland,* [2] *United States Geological Survey, Volcanic Hazards Program, Menlo Park, CA, United States*

Large-volume silicic volcanism poses global hazards in the form of proximal pyroclastic density currents, distal ash fall and short-term climate perturbations, which altogether warrant the study of how silicic magma bodies evolve and assemble. The southern rocky mountain volcanic field (SRMVF) is home to some of the largest super-eruptions in the geological record, and has been studied to help address the debate over how quickly eruptible magma batches can be assembled–whether in decades to centuries, or more slowly over 100's of kyr. The present study focuses on the San Luis caldera complex within the SRMVF, and discusses the paradigms of rapid magma generation vs. rapid magma assembly. The caldera complex consists of three overlapping calderas that overlie the sources of three large-volume mid-Cenozoic ignimbrites: first, the Rat Creek Tuff (RCT; zoned dacite-rhyolite, 150 km^3), followed by the Cebolla Creek Tuff (mafic dacite, 250 km^3) and finally, the Nelson Mountain Tuff (NMT; zoned dacite-rhyolite, 500 km^3), which are all indistinguishable in age by $^{40}Ar/^{39}Ar$ dating. We argue for a shared magmatic history for the three units on the basis of (1) similar mineral trace element compositions in the first and last eruptions (plagioclase, sanidine, biotite, pyroxene, amphibole, titanite, and zircon), (2) overlapping zircon U-Pb ages in all three units, and (3) similar thermal rejuvenation signatures visible in biotite (low-Mn, high-Ba) and zircon (low-Hf, low-U) geochemistry within the RCT and NMT. It is postulated that the NMT was sourced from a pre-existing magma reservoir to the northeast, which is corroborated by the formation of the nearby Cochetopa Caldera during the eruption of the NMT. The inferred lateral magma transport has two important implications: (1) it demonstrates long-distance transport of highly viscosity magmas at volumes (100's of km^3) not previously recorded, and (2) the sourcing of magma from a nearby *pre-existing* magma reservoir greatly reduces the rate of magma generation necessary to explain the close coincidence of three overlapping, large-volume magma systems. Additionally, the concept of magmatic "flux" ($km^3\ kyr^{-1}$) is discussed in this context, and it is argued that an area-normalized flux ($km^3\ kyr^{-1}\ km^{-2}$) provides a more useful number for measuring magma production rates: it is expected that magmatic volumes will scale with footprint of the thermal anomaly, and not taking this into account may lead to errant volumetric

Edited by:
Luis E. Lara, Sernageomin, Chile

Reviewed by:
Jacqueline Vander Auwera, University of Liège, Belgium
Katy Jane Chamberlain, University of Derby, United Kingdom

***Correspondence:**
Jakub Sliwinski
jakub.sliwinski@erdw.ethz.ch

Specialty section:
This article was submitted to Volcanology, a section of the journal Frontiers in Earth Science

Received: *20 June 2019*
Accepted: *02 October 2019*
Published: *25 October 2019*

Citation:
Sliwinski J, Farsky D, Lipman PW, Guillong M and Bachmann O (2019) Rapid Magma Generation or Shared Magmatic Reservoir? Petrology and Geochronology of the Rat Creek and Nelson Mountain Tuffs, CO, USA. Front. Earth Sci. 7:271. doi: 10.3389/feart.2019.00271

flux (km^3 kyr^{-1}) estimates. Meanwhile, area-normalized flux estimates in a given area are similar between units, consistent with evolution in a relatively constant thermal regime. Such estimates also demonstrate similar fluxes for ∼cogenetic volcanic and plutonic units.

Keywords: zircon geochronology, magma rejuvenation, large silicic magma bodies, LA-ICP-MS, mineral chemistry, super eruption, magma flux, biotite chemistry

INTRODUCTION

While volcanism clearly attests to the transit of heat and mass through the earth's crust, the rate at which this process occurs and the details of the mechanism by which the most viscous and explosive magmas evolve remain contentious. Most agree that such magmas are dominantly derived from extensive, fractional-crystallization-driven, long-lived "mushy" reservoirs (Hildreth, 2004), as demonstrated by thermal models (Dufek and Bachmann, 2010; Gelman et al., 2013; Karakas et al., 2017), geochronology (Schmitt et al., 2010; Schoene et al., 2012; Wotzlaw et al., 2013; Cooper et al., 2014; Barboni et al., 2015; Szymanowski et al., 2017) and petrology/geochemistry (Deering and Bachmann, 2010; Pamukcu et al., 2013; Ellis et al., 2014; Wolff et al., 2015; Holness et al., 2019). Such reservoirs, in addition to generating large-volume, crystal-rich ignimbrites, produce crystal-poor eruptible melt batches through slow extraction over 10's to 100's of kyr (Bachmann and Bergantz, 2004; Bachmann and Huber, 2018; Jackson et al., 2018), though many contend that such melt-dominant reservoirs are ephemeral, and the production of large volumes therefore necessitates rapid assembly from smaller melt lenses (Annen, 2009; Wilson and Charlier, 2009; Druitt et al., 2012; Allan et al., 2013; Caricchi et al., 2014; Wotzlaw et al., 2014; Cooper et al., 2017; Flaherty et al., 2018; Shamloo and Till, 2019). Such reservoirs may be prone to rapid cooling and storage in a sub-solidus state (Cooper and Kent, 2014) but the generation of hundreds to thousands of cubic kilometers of eruptible magma would then necessitate high magmatic fluxes (as opposed to incubation; see Mills and Coleman, 2013; Caricchi et al., 2014) in contradiction with results of thermo-mechanical models of magma chambers (Jellinek and DePaolo, 2003; Degruyter et al., 2016). In addition, the controversy surrounding the rates and modes of magmatic melt assembly is compounded by the uncertainty about *lateral* magma migration, which may augment the apparent rates of magma supply to a Volcanic Province (Gutiérrez et al., 2018).

In light of recent models arguing for extensive upper crustal mush zones in *thermally mature crust* heated by lower crustal input (Karakas et al., 2017), along with a growing body of research to support the existence of interconnected upper-crustal magma bodies (Gravley et al., 2007; Bachmann and Huber, 2016; Flinders and Shen, 2017; Brothelande et al., 2018) and lateral magma transport (Curtis, 1968; Hildreth, 1991), it stands to reason that lateral magma transfer is not only possible, but perhaps a critical mechanism for magma assembly. For instance, San Luis caldera complex of the southern rocky mountain volcanic field (SRMVF) experienced three large-volume ignimbrites within 100 ka, which has previously been interpreted as evidence for high magmatic flux (Lipman and McIntosh, 2008), but must be reconsidered in light of evidence for lateral magma transport. In the present study, we reevaluate the significance of this process in the San Luis caldera complex, and expand the discussion to include implications for silicic magma production rates and mechanisms, particularly where integrated magma reservoirs, and lateral magma migration are involved. Additionally, we investigate the crystal cargoes of the first and last eruptions in this sequence (the Rat Creek and Nelson Mountain Tuffs) using a combination of mineral trace element geochemistry and zircon U-Pb geochronology to argue for shared petrogenesis as well as a similar style of magmatic rejuvenation resulting in authogenic cumulate melting.

Geological Background

The central San Juan caldera cluster produced 9 voluminous (>100 km^3) zoned and unzoned ignimbrites in the mid-Cenozoic (Lipman, 2000), beginning with the Masonic Park Tuff (500 km^3 mafic dacite, 28.7 Ma), and proceeding to erupt the Fish Canyon Tuff [5,000 km^3 dacite, 28.02 Ma; (Bachmann et al., 2002)], the Carpenter Ridge Tuff (1,000 km^3 zoned dacite-rhyolite, 27.55 Ma), the Blue Creek Tuff (250 km^3 dacite, 27.4 Ma), the Wason Park Tuff (500 km^3 zoned dacite-rhyolite, 27.35 Ma) and, in its waning stages, the San Luis caldera complex and the slightly younger Snowshoe Mountain Tuff [500 km^3 mafic dacite, 26.85 Ma; see **Figure 1**; Lipman and Bachmann, 2015]. Ignimbrites erupted from the San Luis caldera complex include (in chronological order): the Rat Creek Tuff (RCT, 150 km^3, rhyolite-dacite with 65–74 wt.% SiO_2), the Cebolla Creek Tuff (CCT, 300 km^3, mafic dacite with 61–64 wt.% SiO_2), and Nelson Mountain Tuff (NMT, 500 km^3, rhyolite-dacite with 63–74 wt.% SiO_2), with bracketing sanidine $^{40}Ar/^{39}Ar$ ages of 26.91 ± 0.02 and 26.90 ± 0.03 Ma for the first and last ignimbrites (respectively), constraining the eruptive duration for all three eruptions to within ∼60 kyr (Lipman and McIntosh, 2008). The three units are separated by eruptive hiatuses, as evidenced by intervening bedded fall/surge deposits and reworked tuffs, local erosive removal of the RCT/CCT by the CCT/NMT and the accumulation of intracaldera lavas between ignimbrites (Lipman, 2000).

Given the diversity in eruptive products in both the RCT and NMT, these two ignimbrites are further subdivided into subunits by composition and degree of welding (see **Figure 1** and **Supplementary Table S1**; Lipman, 2006). The RCT grades from a dominantly non-welded crystal-poor white-yellow pumiceous tuff (*Trr*) to a crystal-rich welded dacite (*Trd*) with color (black-brown) associated with variable degrees of devitrification. The NMT, with larger volume and more extensive distribution has a greater number of subdivisions (Lipman, 2006), a number

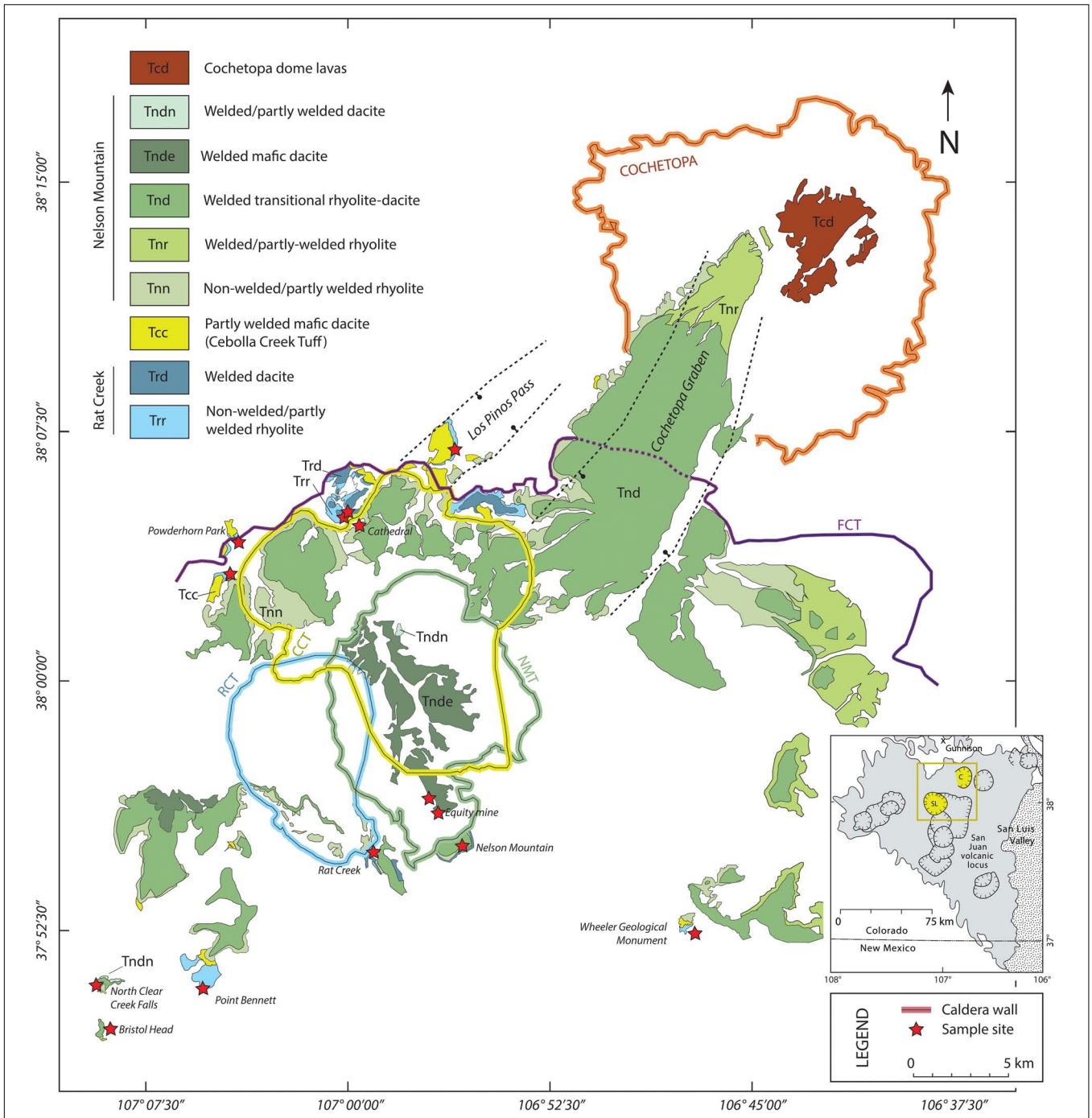

FIGURE 1 | Geologic map of the San Luis complex and Cochetopa Park calderas (Lipman, 2006), showing the preserved distribution of NMT (green), RCT (blue), and CCT (yellow) ignimbrites as well as the unconformities that define their source caldera margins (including Fish Canyon Tuff, FCT) and stars denoting sample sites. Inset: Simplified map of the San Juan magmatic locus within the SRMVF near the Colorado/New Mexico border (Lipman and McIntosh, 2008), showing the distribution of calderas, the extent of mid-Cenozoic volcanic rocks in gray, younger fill of the San Luis Valley in stippled pattern, and location of the San Luis-Cochetopa map. SL, San Luis; C, Cochetopa. Ignimbrite preservation extends further to the SW but is not pictured here. For ignimbrite descriptions, see **Table 1**.

of which are pertinent to this study. Namely, a basal non-welded to partly welded pumiceous crystal-poor rhyolitic tuff (*Tnn*), similar to *Trr,* is overlain by a welded to partly welded crystal-poor rhyolite (*Tnr*), which in turn grades into a welded crystal-rich silicic dacite (*Tnd*) in the outflow tuffs. Preserved within the caldera, stratigraphically above these subunits are a welded crystal-rich mafic dacite (*Tnde*) and a partly welded crystal-rich dacite (*Tndn*), the latter of which is also preserved

locally atop proximal outflow tuff. The intervening CCT is dominantly a partly welded mafic dacite (*Tcc*) between the NMT and/or RCT, with the three tuffs especially prominent at the Wheeler Geological Monument.

The three ignimbrites are similar in phenocryst assemblage, each with some variation of plagioclase ± sanidine + biotite + clinopyroxene + Fe-Ti-oxides + zircon + apatite ± quartz ± titanite ± amphibole (e.g., see **Supplementary Figure S1**), with notable exceptions: sanidine is absent from the CCT, which makes the $^{40}Ar/^{39}Ar$ age difficult to precisely constrain. Amphibole is the dominant ferromagnesian phase in the CCT, as well as an accessory phase together with clinopyroxene in the uppermost NMT (*Tnde* and *Tndn*) as well as throughout the RCT (*Trr, Trd*). Orthopyroxene is rare and is typically associated with evidence of mafic recharge.

The San Luis caldera complex is connected by the Cochetopa and Los Pinos grabens to the Cochetopa Park caldera, 25 km to the northeast (**Figure 1**; Lipman, 2000). Curiously, no sizable ignimbrite erupted *directly* from this large caldera (∼20 × 25 km), with the intracaldera volcanics limited to a lobe of the Nelson Mountain Tuff that flowed in from the SW along the Cochetopa Graben, small-volume pyroclastic-flow and –fall tuffs, and lavas of the Cochetopa Dome Rhyolite (∼75–77 wt.% SiO2; see Lipman, 2012). Regardless, the lateral extent of this

TABLE 1 | Sample locations and data summary.

Sample	Mapped unit	Latitude	Longitude	Locality, notes	XRF	Glass	Feldspar	Biotite	Pyroxene	Amphibole	Titanite	Zircon
Nelson mountain dacite												
17SJ02	*Tndn*	37°51'01"	107°08'58"	North clear creek falls	x	o	x	x	x	o	x	x
17SJ18	*Tnde*	37°55'59"	106°57'33"	Equity mine	x	o	x	x	o	o	o	x
17SJ03	*Tnd*	37°51'01"	107°08'58"	North clear creek falls	x	o	x	x	x	x	x	x
NMT14-1	*Tnd*	37°50'55"	106°08'50"	North clear creek falls	x	o	x	x	x	x	N/A	x
17SJ09	*Tnd*	37°54'52"	106°56'06"	Nelson mountain	x	o	x	x	x	o	x	x
NMT08-2	*Tnd*	37°52'49"	106°46'01"	Wheeler monument	x	o	N/A	X	N/A	N/A	N/A	N/A
Nelson mountain rhyolite												
17SJ17	*Tnr*	37°54'28"	106°57'21"	Equity mine	x	o	x	x	o	o	o	x
17SJ04	*Tnn*	37°49'01"	107°08'04"	Bristol head	x	o	x	x	x	o	x	x
NMT14-2	*Tnn*	37°49'01"	107°08'04"	Bristol head	x	x	x	x	x	N/A	x	x
17SJ16	*Tnn*	38°04'35"	107°00'24"	Powderhorn park	x	o	x	x	o	o	x	x
17SJ19	*Tnn*	38°04'53"	107°05'02"	Powderhorn park	x	o	x	x	x	o	x	x
NMT08-1	*Tnn*	37°52'49"	106°46'01"	Wheeler monument	x	N/A	N/A	N/A	N/A	N/A	x	N/A
Cebolla creek tuf												
SRM07	*Tcc*	38°05'47"	106°59'04"	Los pinos pass	N/A	N/A	N/A	N/A	N/A	N/A	N/A	x
Rat creek dacite												
RCT14-1	*Trd*	37°54'41"	106°58'58"	Rat creek	x	o	x	x	x	o	x	x
17DF13	*Trd*	38°04'55"	107°00'07"	Cathedral creek	x	o	x	x	x	x	x	x
17DF12	*Trd*	38°04'53"	107°00'08"	Cathedral creek	x	o	x	x	x	x	x	x
17DF09	*Trd*	38°04'50"	107°00'05"	Cathedral creek	x	o	N/A	N/A	N/A	N/A	N/A	N/A
Rat creek rhyolite												
17DF11	*Trr*	38°04'51"	107°00'06"	Cathedral creek	x	o	x	x	x	x	x	x
17DF10	*Trr*	38°04'50"	107°00'05"	Cathedral creek	x	o	x	x	o	x	x	x
17DF08	*Trr*	38°04'50"	107°00'05"	Cathedral creek	x	o	N/A	N/A	N/A	N/A	N/A	N/A
17DF06	*Trr*	38°03'47"	107°04'30"	Powderhorn park	x	o	N/A	N/A	N/A	N/A	N/A	N/A
17DF15	*Trr*	38°07'44"	106°56'22"	Los pinos creek	x	o	N/A	N/A	N/A	N/A	N/A	N/A
17DF01	*Trr*	37°52'43"	106°47'07"	Wheeler monument	x	o	x	x	x	o	x	x
17DF21	*Trr*	37°51'17"	107°05'48"	Point bennett	x	o	N/A	N/A	N/A	N/A	N/A	N/A
Rat creek pumice*												
17DF18	*Trrg*	38°4'44"	106°56'22"	Los pinos creek	x	o	N/A	N/A	N/A	N/A	N/A	N/A
15SJ14	*Trrg*	38°4'44"	106°56'22"	Los pinos creek	x	x	x	x	x	o	N/A	x
17DF20-1	*Trrf*	38°4'44"	106°56'22"	Los pinos creek	x	x	x	x	x	o	o	x
17DF20-2	*Trrf*	38°4'44"	106°56'22"	Los Pinos Creek	x	o	x	x	x	o	o	x
17DF20-3	*Trrf*	38°4'44"	106°56'22"	Los pinos creek	x	o	x	x	x	o	o	x
17DF19-1	*Trrm*	38°4'44"	106°56'22"	Los pinos creek	x	x	x	x	x	o	o	x
17DF19-2	*Trrm*	38°4'44"	106°56'22"	Los pinos creek	x	o	x	x	x	o	o	x
17DF19-3	*Trrm*	38°4'44"	106°56'22"	Los pinos creek	x	o	x	x	x	o	o	x

**Defined in this study: Trrg = mingled pumice or mixed pumice sample, RCT; Trrf = "felsic" white pumice, RCT; Trrm = "mafic" dark pumice, RCT; Data: x = analysis performed; o = phase not present; N/A = no attempted search.*

caldera and the degree of subsidence (∼300–800 m) suggests that it formed following the evacuation of 100's of km^3 of magma. This led Lipman and McIntosh (2008) to postulate that the subsidence at Cochetopa resulted from the lateral transport of Nelson Mountain Tuff magma prior to its eruption from within the San Luis complex. Such a process has been observed during the 1912 Katmai-Novarupta eruption (Hildreth, 1991) and in the Taupo Volcanic Zone (Gravley et al., 2007; Allan et al., 2013), but remains rarely documented in the volcanological record.

MATERIALS AND METHODS

Sampling Rationale

Samples were collected in summer 2017 and supplemented with archived rocks in order to cover the most prominent subunits of the RCT and NMT, including both the rhyolitic and dacitic subunits and subunits with different degrees of welding. In order to obtain meaningful XRF and mineral data, samples were chosen that had as few lithic clasts as possible. Pumices were collected from the *Tnn* (samples 17SJ04, NMT08-1 and NMT14-2) as well as *Trr* (15SJ14, 17DF18-20). A single sample of CCT was collected for zircon U-Pb dating. For more details, see **Table 1**, **Supplementary Tables S1**, **S2**, and **Supplementary Figure S10**.

Whole Rock Geochemistry

Whole rock major and trace element chemistry were determined from bulk ignimbrite samples and pumices (where noted). Glass beads that were fused from milled and homogenized powders using a 1:5 mass ratio of sample to lithium tetraborate (or metaborate) flux at ETH Zürich. Thirty-one samples were analyzed using a PANalytical Axios wavelength-dispersive X-ray fluorescence spectrometer for major elements and laser ablation inductively coupled-plasma mass spectrometry (LA-ICP-MS) for trace elements (see below for details). Loss on ignition was calculated following a 2 h devolatilization period at 1050°C prior to glass fusing. Typical analytical uncertainties amount to 0.2–0.5% for major elements (relative, 2σ), and ∼5% for trace elements that with concentrations at least 2–3 times greater than the limit of detection (LOD).

Mineral and Glass Chemistry

Mineral chemistry was determined from both polished petrographic thin sections and grain mounts through a combination of energy dispersive x-ray spectroscopy [EDS; Thermo Fisher Ultra Dry Detector SDD/Noran systems EDS paired with a JEOL JSM-6390 scanning electron microscope (SEM)] and LA-ICP-MS (193 nm ArF excimer laser from ASI paired with a Thermo Element XR mass spectrometer). Typical analytical conditions for EDS measurements consisted of 15 kV acceleration voltage, ∼3 nA beam current, 25–29% downtime and a ∼1 μm beam size. Long-term data trends indicate an agreement between EDS and electron microprobe analyses (Allaz et al., 2019) and a relative precision on major element concentrations better than 5% (**Supplementary Table S4**).

Major element data from EDS were used for internal standardization of LA-ICP-MS trace element analyses, using either Al, Ca or Si (depending on the mineral) to anchor the raw data to precise concentrations. Here, standardization was performed relative to the NIST-610 synthetic glass standard using consistent analytical parameters (3.5 J cm^{-2}; 5 Hz repetition rate; 30 μm spot size; 40 s ablation time, 30 s gas blank). Concentrations were verified using a GSD-1G synthetic basalt as a secondary standard.

For temperature estimates, the Ti-in-zircon geothermometer was used (Ferry and Watson, 2007), using Ti concentrations (μg g^{-1}) obtained by LA-ICP-MS and assuming constant $a_{TiO2} = 0.7$ and $a_{SiO2} = 1.0$. The SiO_2 activity is based on the presence of quartz in most samples, and it is assumed that when quartz is absent, this is due to resorption during rejuvenation (similar to the preceding Masonic Park Tuff, see Sliwinski et al. (2017a). The TiO_2 activity is selected to be similar to the Fish Canyon Tuff (Ghiorso and Gualda, 2013), which has a very similar mineralogy that also includes titanite.

U-Pb Dating

Zircon U-Pb ages were obtained by LA-ICP-MS using the same setup as for trace elements, and were obtained following thermal annealing and/or chemical abrasion (Mattinson, 2005). Zircon grains where sectioned to expose interior zones, and then polished to a 1 μm finish with a diamond suspension. Data were reduced using Iolite v2.5 (Paton et al., 2011) and the VizualAge data reduction scheme (Petrus and Kamber, 2012) by normalizing U-Pb ratios of the GJ-1 calibration reference material to its established ID-TIMS value (Horstwood et al., 2016). Data accuracy and systematic bias were monitored using an array of validation reference materials: Temora2 (Black et al., 2004), 91500 (Wiedenbeck et al., 1995), OD-3 (Iwano et al., 2013), and Plesovice (Sláma et al., 2007). Because of the large degree of systematic uncertainty common to the method [approaching 2%, compared to an intra-session optimum of 0.5% relative uncertainty on the $^{206}Pb/^{238}U$ age; see Horstwood et al. (2016)], comparisons between zircon populations were made by analyzing them on the same day. When sufficient validation reference materials were analyzed, an alpha radiation dose correction was applied to correct for anomalously young ages. For more details and analytical parameters, see **Supplementary Table S3** and Sliwinski et al. (2017c).

RESULTS

Bulk Rock and Glass Chemistry

The Nelson Mountain and Rat Creek Tuffs are remarkably heterogeneous in outcrop as well as bulk chemistry. The rhyolitic base of the RCT at Point Bennett is texturally and chemically indistinguishable from other instances of the unit (*Trr,* see legend in **Figure 1** for simplified stratigraphy), with 69–74 wt.% SiO_2 (normalized, anhydrous; **Supplementary Table S4**), consistent with published values (Lipman, 2004). The only exception in this study is at the top of the section at Cathedral Creek, where the unit is distinctly welded directly underlying the dacitic member (*Trd*). Here, the dacitic RCT is almost exclusively welded and crystal-rich with bulk SiO_2 between 64 and 69 wt.%, and a Eu anomaly (Eu/Eu*, using a geometric mean of Sm and Gd) that is subdued relative to the rhyolitic member

(**Supplementary Figure S2**). This difference in Eu anomaly and bulk SiO_2 content is reflected in the chemistry of the pumices, nicely preserved at Los Pinos Creek as two distinct varieties of pumice ["mafic" and "felsic," defined here as *Trrm* and *Trrf* for consistency with (Lipman, 2000)], with the "mafic" pumice mirroring the dacitic bulk chemistry (68–69 wt. % SiO_2) and the "felsic" pumice overlapping the rhyolitic bulk chemistry (68–73 wt. % SiO_2). Mingled pumices and mixed pumice samples (*Trrg*) show predictably intermediate values, although one mixed pumice sample (15SJ14) has unusually low SiO_2 (64 wt. %) likely caused by contamination by mafic enclaves as evidenced by the presence of rare orthopyroxene phenocrysts.

Pumices of the Nelson Mountain Tuff are similarly rhyolitic (70–72 wt. % SiO_2) and feature prominently in the crystal-poor non-welded member (*Tnn*), which has a corresponding *bulk* SiO_2 range of 69–75 wt. % and grades into a crystal-poor welded tuff (*Tnr*, 72 wt. % SiO_2). This unit grades upward into a crystal-rich welded silicic dacite (*Tnd,* 63–67 wt. % SiO_2), which in turn lies stratigraphically below the crystal-rich intracaldera welded member near Equity Mine (*Tnde*, 67 wt. % SiO_2). Rarest and highest in the stratigraphy is a partly welded crystal-rich dacite (*Tndn,* 66 wt. % SiO_2) sampled outside the inferred caldera walls at North Clear Creek Falls. As with the RCT, the strength of the Eu anomaly correlates with the bulk SiO_2 content, with rhyolitic members showing more pronounced anomalies (**Figure 2** and **Supplementary Figure S2**), consistent with published values (**Supplementary Figure S3**; Streck, 2014).

Pumice glass from the NMT and RCT is rhyolitic with 71–78 wt. % SiO_2 (normalized, anhydrous) in two clusters (see **Figure 2**, **Supplementary Figure S4**, and **Supplementary Table S4**): NMT glass is broadly similar to "felsic" pumice glass (*Trrf*) from the RCT, with 75–78 wt. % SiO_2, Eu/Eu* = 0.4–0.6, 0.1–1 wt. % FeO, 8–10 wt.% $Na_2O + K_2O$ and 12–14 wt. % Al_2O_3, while "mafic" pumice glass (*Trrm*) contains 71–74 wt. % SiO_2, Eu/Eu* = 0.7–0.9, 1–1.6 wt. % FeO, 9–10 wt.% $Na_2O + K_2O$ and 14–15 wt. % Al_2O_3. This "mafic" glass is also characterized by increased Sr and Ba relative to the "felsic" group (185 vs. 35 $\mu g\ g^{-1}$ Sr and 2,000 vs. 270 $\mu g\ g^{-1}$ Ba, respectively). Meanwhile, glass from the NMT is slightly less silicic than the "felsic" RCT pumice (76 vs. 77.5 wt.% SiO_2 average) with correspondingly lower Rb and Nb concentrations (137 vs. 172 $\mu g\ g^{-1}$ and 17 vs. 19 $\mu g\ g^{-1}$, respectively) indicating a lower degree of fractional crystallization. For more compatible elements (Ba, Sr), concentrations in these two units are broadly quite similar.

Feldspar Chemistry

Feldspars are present as fragmented euhedral phenocrysts of plagioclase and sanidine in both the RCT and NMT, with substantial variations in chemical composition within each unit (**Figure 3**, **Supplementary Figure S1**, and **Supplementary Table S4**). While both feldspars are present in all samples, low abundances or small phenocryst sizes preclude their analysis in some cases (e.g., sanidine was not analyzed in dacitic *Tnd* and one *Trd* sample, nor was plagioclase in rhyolitic *Tnr)*. Rhyolitic RCT plagioclase varies between An_{20} and An_{30}, with the exception of the "mafic" pumice, which has An_{37-47}. This range in compositions overlaps with dacitic RCT plagioclase (An_{35-40}), which are in turn indistinguishable from dacitic NMT plagioclase phenocrysts. Rhyolitic NMT plagioclase shows wide variability, overlapping with both dacitic populations with An_{30-45}. Sanidine presents dominantly in the rhyolitic units, and shows strong coherence in Or content between rhyolitic and dacitic RCT samples with Or_{60-65}. Rhyolitic NMT shows more spread in sanidine compositions, ranging from Or_{57} to Or_{65}, while rare sanidines in dacitic NMT show increased K content (Or_{65-75}).

Trace element concentrations vary strongly between subunits as well as within individual crystals, with many phenocrysts displaying normal and oscillatory zoning patterns in backscatter electron (BSE) imaging, indicative of significant Sr and Ba variations. The late-erupted RCT dacite shows pronounced increases in sanidine Ba content (1–2 wt. % Ba) as well as plagioclase Sr content (1,500–2,500 $\mu g\ g^{-1}$) relative to other subunits. Similar trends are seen in pumice glass of the RCT (*Trrf* and *Trrm*, **Figure 2**).

Biotite Chemistry

Biotite major element chemistry is consistent with that published elsewhere in the SRMVF [e.g., the Fish Canyon Tuff, see Bachmann and Bergantz (2003)], although trace element chemistry demonstrates considerably more heterogeneity. While major element chemistry is relatively constant with 7–9 wt. % K_2O, 12–14 wt. % Al_2O_3 and Mg/(Mg + Fe) ratios of 0.5–0.7 (**Supplementary Table S4**), BSE imaging reveals pronounced resorption and recrystallization textures corresponding to increased Ba concentrations, particularly in pumices. This variability can be linked to variations in other trace elements, which in turn demonstrate pronounced variability when compared to other units in the SRMVF.

The majority of biotites from dacitic units and subunits in the San Juan locus (including the Carpenter Ridge Tuff, Fish Canyon Tuff, and San Luis units from this study) contain relatively constrained V, Co, and Mn concentrations (**Figures 4a–c**) which are markedly different from more differentiated units. The sum of all units defines a fractionation trend (e.g., see Nandedkar et al., 2014) whereby V and Co decrease with increasing bulk SiO_2 concentration (e.g., the Wason Park Tuff and rhyolitic RCT and NMT), while Mn rises due to its bulk incompatibility (Watson, 1977; Hirschmann and Ghiorso, 1994). The Masonic Park and Snowshoe Mountain Tuffs (coincidentally the first and last units in the caldera complex) appear to contain more primitive biotites with Mn concentrations fivefold lower than in the rhyolitic NMT and RCT. However, RCT and NMT biotites from bulk rhyolites demonstrate a bimodality in composition (**Figure 4a**), with a portion containing only ~2,000 $\mu g\ g^{-1}$ Mn (compared with 5,000 $\mu g\ g^{-1}$) at similar V and Co concentrations, and on average threefold higher Ba concentrations (**Figure 4b**).

The same variability in Mn can be observed within the RCT pumices (*Trrm* and *Trrf*), with the "felsic" pumice containing exclusively high Mn and the "mafic" pumice containing exclusively low Mn (**Figure 4d**). These compositions overlap with welded *Trr* and *Trd* compositions (respectively), while non-welded *Trr* biotites contain a fully bimodal population similar to that of the non-welded *Tnn* (NMT; **Figure 4a**).

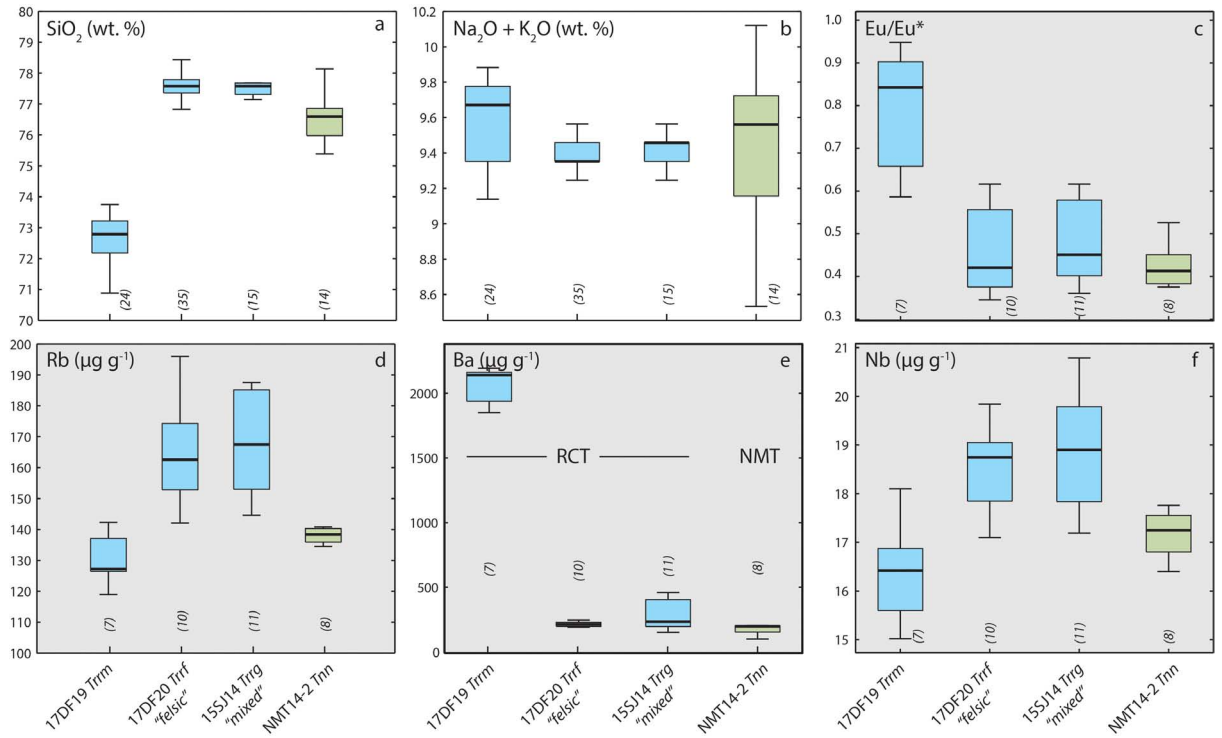

FIGURE 2 | Select major and trace element concentrations in RCT and NMT glass: **(top)** SiO_2, $Na_2O + K_2O$ (wt.%) and Eu/Eu*, demonstrating a pronounced difference between "mafic" RCT glass (*Trrm*) and the remaining RCT and NMT glass; **(bottom)**: Rb, Ba, and Nb concentrations (µg g^{-1}), with *Trrm* showing increased Ba and decreased Rb. Major elements normalized to 100% anhydrous. See **bottom middle panel** for sample labels and x-axis labels (number of analyses represented by numbers in parentheses). Boxes represent median and 1st/3rd quartiles; whiskers represent the 10th and 90th percentiles.

Clinopyroxene and Amphibole

Clinopyroxenes are present in nearly all NMT and RCT samples (though notably absent in the CCT) as subhedral to partly resorbed phenocrysts, with relatively consistent major element compositions of Mg_{72-75}, 21–23 wt.% CaO (**Supplementary Figure S5** and **Supplementary Table S4**). Dacitic NMT and RCT additionally demonstrate a consistent Eu/Eu* of ∼0.4 and REE sums of ∼200 µg g^{-1}, while rhyolitic units contain a broader range in both parameters (0.4–0.7 and 0–300, respectively). Rare orthopyroxene appears in the "mafic" pumice of the RCT (*Trrm)* as well as the rhyolitic NMT (*Tnn*).

Whereas the CCT contains abundant amphibole and no pyroxene, the NMT and RCT contain both phases (though predominantly pyroxene). Mg-hornblende-hastingsite features prominently in the rhyolitic and dacitic subunits of the RCT (*Trr* and *Trd*), as well as in the dacitic NMT (*Tnd*). Phenocrysts are not strongly zoned, and variability in Al_2O_3 between grains suggests sourcing from various depths: welded RCT (*Trr* and *Trd)* from Cathedral Creek contain amphiboles with 12–13 wt.% Al_2O_3 and Mg_{65-70} (**Figure 5**, **Supplementary Figure S6**, and **Supplementary Table S5**), yielding an approximate temperature and pressure of ∼400 MPa and ∼1,000°C (respectively), using the geobarometer of Ridolfi et al. (2010). Meanwhile, non-welded *Trr* contains a range in Al_2O_3 from 6–13 wt.% with Mg_{65-70}, both overlapping with NMT samples at <200 MPa and <900°C (indicating shallower crystallization and mixing of the magma prior to eruption; **Supplementary Figure S6**). It should be noted that while the low-Al amphiboles overlap in composition with the archetypal Fish Canyon Tuff [5–9 wt.% Al; Bachmann and Dungan (2002)] and the CCT (M. Myers, *personal communication*), the high-Al amphiboles are suggestive of deeper/hotter origin, possibly due to entrainment of xenocrysts or recharge-crysts. The geobarometry data in this study are not combined with any other mineral geobarometers (e.g., Blundy and Holland, 1990; Anderson and Smith, 1995), and the interpretation of the results should therefore be treated with caution (see, for example, Kiss et al. (2014) and Erdmann et al. (2014) for discussion about issues using amphibole barometry).

Zircon and Titanite

Zircons are ubiquitous in SRMVF units and are particularly abundant in crystal-rich units where they additionally display a diverse array of oscillatory and sector zoning (**Figure 6b**) patterns as well as variations in cathodoluminescence (CL) brightness indicative of variable trace element concentrations (U, Th, REE, and Hf). These variations fall within certain restricted limits for the majority of zircons (8,000–11,000 µg g^{-1} Hf, 100–500 µg g^{-1} U, Eu/Eu* = 0.2–0.5, Yb/Dy = 3–6; **Figures 6c–e**), with the exception of subsets of zircons from the RCT and NMT pumices. Here, a marked decrease in Hf (5,000–7,000 µg g^{-1}) and U (∼100 µg g^{-1}) are paired with an increased

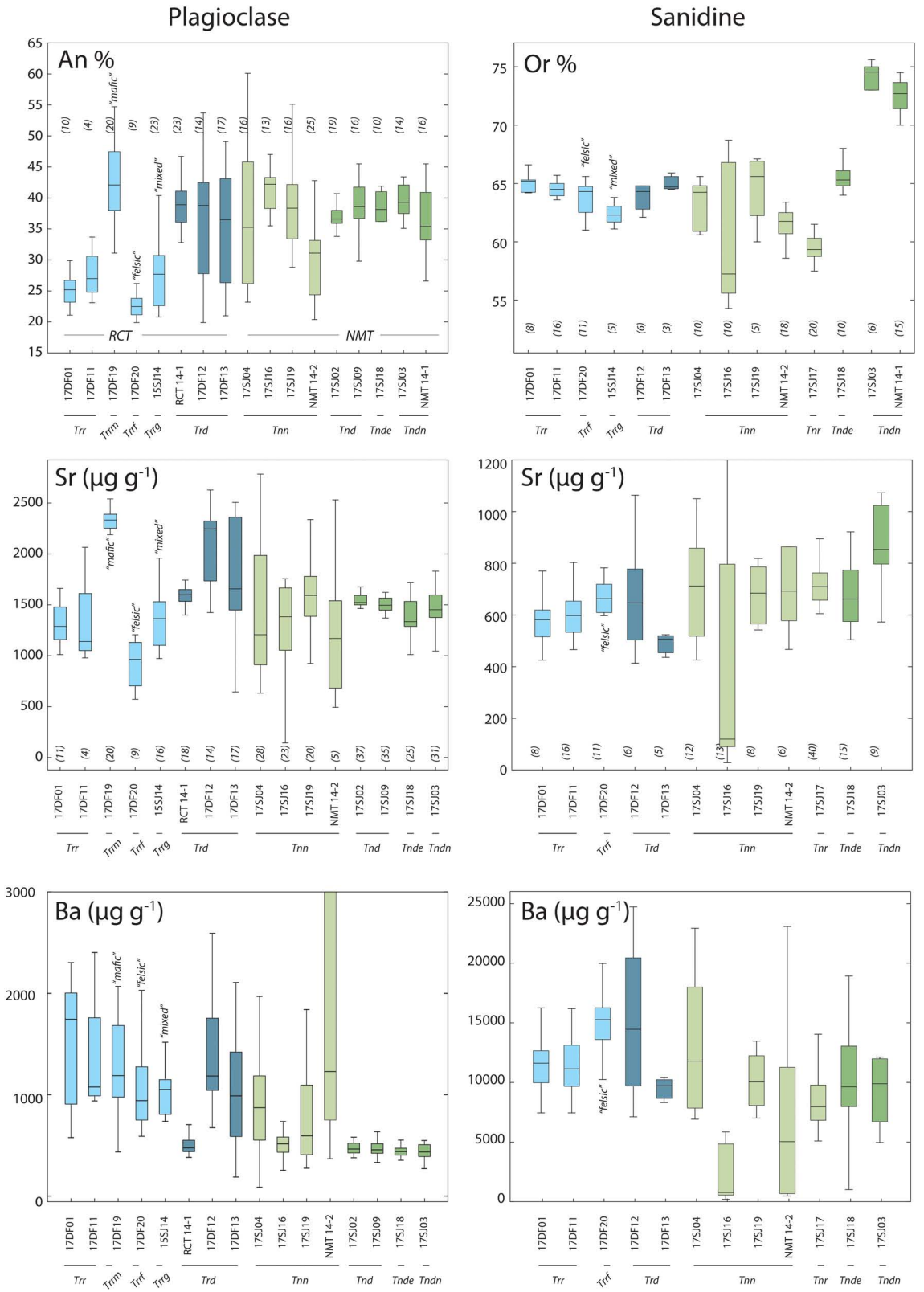

FIGURE 3 | Plagioclase **(left)** and sanidine **(right)** major and trace element (Sr, Ba) chemistry for the RCT and NMT: **(top)** An of plagioclase and Or of sanidine. See **Figure 1** and **Table 1** for unit descriptions. Shades of blue are NMT; shades of green are RCT (dark, dacitic; light, rhyolitic for both). Boxes represent median and 1st/3rd quartiles; whiskers represent the 10th and 90th percentiles; number of analyses in parentheses.

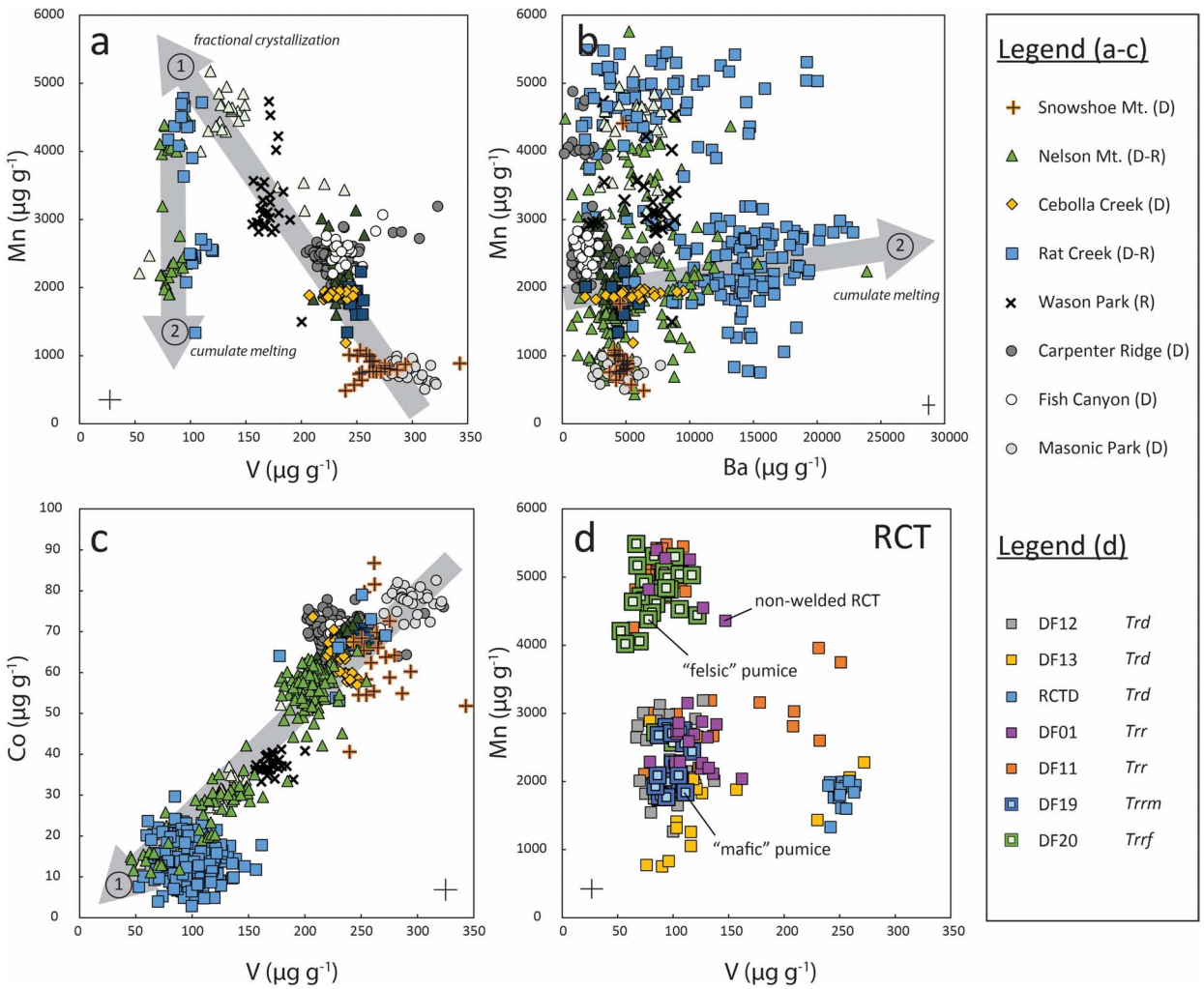

FIGURE 4 | Biotite trace element variations among central San Juan ignimbrite units (D, dacite; R, rhyolite) in comparison with the San Luis cluster: **(a)** Mn vs. V (ppm), demonstrating both a fractionation trend (arrow 1) and the effect of feldspar melt-doping (arrow 2). Some data from RCT and NMT excluded for clarity. **(b)** Mn vs. Ba, demonstrating Ba enrichment among low-Mn RCT and NMT samples. **(c)** Co vs. V for all central San Juan biotites, demonstrating a fractionation trend. **(d)** Mn vs. V for individual RCT samples, demonstrating two distinct groups correlated with the compositions of "mafic" and "felsic" pumices. Different shades of symbols signify different samples within the same unit. Error bars show conservative ~5% 2 s uncertainty, based on long-term reproducibility of reference materials.

Eu/Eu* of ~0.6–0.7. Decreased Hf and U are suggestive of increased crystallization temperatures, and the two are negatively correlated with Ti (**Supplementary Figure S7**). Finally, decreased Yb/Dy is consistent with crystallization in the absence of titanite, which preferentially incorporates middle REE's and increases the ratio (Wotzlaw et al., 2013).

Where available, Ti-in-zircon temperatures (Ferry and Watson, 2007) demonstrate wide variability within units, likely due to mixing of zircon populations by magma homogenization. Zircons from the dacitic and rhyolitic NMT (*Tnn, Tnd, Tnde*, and *Tndn*) show essentially overlapping zircon temperatures with sample medians between 760 and 800°C, assuming a_{TiO2} = 0.7 and a_{SiO2} = 1.0 (**Figure 7**). Due to smaller sample sizes, RCT zircons show more variability in the rhyolitic and dacitic subunits (*Trr* and *Trd*), but essentially fall within the same limits. The RCT pumice zircons, meanwhile, show a marked and tightly constrained temperature increase (840–860°C), correlated with changes in Eu/Eu*, Hf, and U mentioned above. The homogeneity of these populations is likely due to the excellent preservation of the juvenile magma without syn-eruptive mixing.

U-Pb ages of zircons from the CCT, and the rhyolitic and dacitic subunits of the NMT and RCT are broadly consistent with one another, with weighted mean ages between 26.52 ± 0.11 (*Trr*) and 27.56 ± 0.25 Ma (*Tnn*). These ages are at first inconsistent with the $^{40}Ar/^{39}Ar$ ages of the units [~26.9 Ma, calibrated to a Fish Canyon Tuff age of 28.02 Ma (Lipman and McIntosh, 2008)], but when corrected with validation reference materials for differences in alpha radiation dosage and Th disequilibrium (Sakata et al., 2017; Sliwinski et al., 2017c), these ages show better agreement with the eruption age (being typically slightly older, as expected from the zircon crystallization age record):

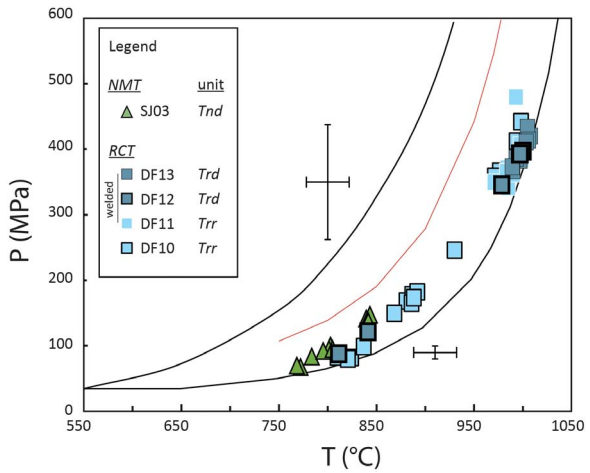

FIGURE 5 | Pressure (MPa) and temperature (°C) estimates for amphibole crystallization, using the geobarometer of Ridolfi et al. (2010). Error bars are schematic 2 s uncertainties.

27.13 ± 0.12 Ma (*Trr*), 27.18 ± 0.11 (*Trd*), 27.56 ± 0.12 (*Tcc*), 27.27 ± 0.15 (*Tnd*), and 28.06 ± 0.23 Ma (*Tnn;* see **Figure 6a**).

Just as San Luis units are consistent in U-Pb zircon ages with one another, individual NMT and RCT samples are also consistent with one another when care is taken to minimize sources of systematic bias (**Supplementary Figure S8**) – with one notable exception. Zircons from pumices in the RCT and NMT demonstrate anomalously young U-Pb ages in addition to their low U, Hf, and REE concentrations described above (**Figure 7**). The young ages are likely not the result of a minimally lower alpha radiation dose, but rather a true anomaly that can be paired with trace element compositions indicative of hotter crystallization conditions. This is corroborated by the absence of co-crystallizing titanite.

Titanite appears in nearly all NMT and RCT units as euhedral-subhedral phenocrysts with complex zoning patterns typical of complex crystallization histories. Application of the Zr-in-titanite thermometer (Hayden et al., 2008) yields consistent titanite crystallization temperatures of 730–750°C, assuming a_{TiO2} = 0.7 and a_{SiO2} = 1.0 as with the zircon thermometer (**Figure 7**). Temperatures are typically lower than zircon temperatures, and more tightly clustered, indicating a narrower range of thermal stability. Titanite is lacking in mafic, felsic and mixed pumices from the RCT (apart from a few resorbed grains in the felsic pumice, excluded as xenocrysts), as well as in welded NMT rhyolite (*Tnr*) and intracaldera NMT dacite (*Tnde*).

DISCUSSION

Magma Rejuvenation in the San Luis Caldera Complex

The eruption of crystal-rich magma in mushy reservoirs often involves a thermal rejuvenation event triggered by the arrival of deeper-hotter recharge, which may leave a variety of markers in the volcanic record. For instance, the Fish Canyon Tuff contains rare andesitic blebs as a testament to late-stage mafic recharge (Lipman et al., 1997), the Masonic Park Tuff contains high-An rims on plagioclase (as well as high An microlites) and an absence of sanidine, titanite and quartz as evidence of strong pre-eruptive heating (Sliwinski et al., 2017a), and the Carpenter Ridge Tuff contains sanidine and biotite phenocrysts with strong Ba enrichment indicative of crystallization from a melt dominated by authogenic feldspar cumulate melt (Bachmann et al., 2014). Globally, a similar record of cumulate "cannibalization" can be seen through bulk rock or mineral chemistry in zoned and unzoned ignimbrites, including the Ammonia Tanks Tuff (Deering et al., 2011), Peach Springs Tuff (Pamukcu et al., 2013), Tenerife (Sliwinski et al., 2015), Bishop Tuff (Evans and Bachmann, 2013; Chamberlain et al., 2014), Bandelier Tuff (Wilcock et al., 2012; Wolff et al., 2015), Kidnappers/Rocky Hill Ignimbrites (Cooper et al., 2017) and Campi Flegrei and Lipari (Forni et al., 2015, 2018a,b). Elsewhere, evidence for high-temperature rejuvenation is seen in chemical diffusion profiles (e.g., Fe-Mg interdiffusion in orthopyroxene, Ti-in-quartz, Sr-in-plagioclase), where sub-decadal to millennial timescales are calculated (Druitt et al., 2012; Cooper et al., 2017; Flaherty et al., 2018).

Rejuvenation is evident in NMT and RCT pumices in the form of anomalous biotite, glass and zircon compositions suggestive of crystallization from cumulate-doped melt. Biotites from both rhyolites contain low Co and V suggestive of high chemical evolution, yet Mn concentrations are exceptionally low (**Figure 4**). This indicates either a lower D_{Mn} caused by depolymerization of the melt, or crystallization from a melt with decreased Mn. Melting of feldspar cumulates accomplishes both criteria: elevated temperatures and addition of Na and K into the melt work to decrease melt polymerization, while low Mn concentrations in feldspar lower the melt Mn content. Additionally, the liberation of Ba by feldspar melting enhances the Ba concentration in biotites grown from these doped melts (**Figure 4b**). The same Ba enrichment is seen in sanidines and in the "mafic" pumice glass of the RCT (*Trrm*, **Figure 2**), which is interpreted to represent the parent melt of these biotite compositions.

Zircons demonstrate the effects of rejuvenation through both chemical composition and age spectra in the rhyolitic RCT and NMT. Decreased Hf and U are both indicative of increased crystallization temperature, along with increased Ti which suggests crystallization temperatures in the range of 840–860°C, well above the rest of the units (**Figure 7**). The increased Eu/Eu* ratio is consistent with crystallization from magma that has been enhanced by feldspar melt, while the decreased Yb/Dy ratio is consistent with the scarcity (i.e., resorption) of titanite from these samples (**Figure 6**). Finally, the ages of these low-U zircons are among the youngest in the population, which together with the temperature data suggests that these zircons formed immediately after the onset of the rejuvenation event that triggered the eruption (**Figure 7**). The similar behavior of these zircons in both units, as well as similarities in biotite and glass rejuvenation signatures, attests to the overall likelihood that they share a common magmatic history, as discussed later.

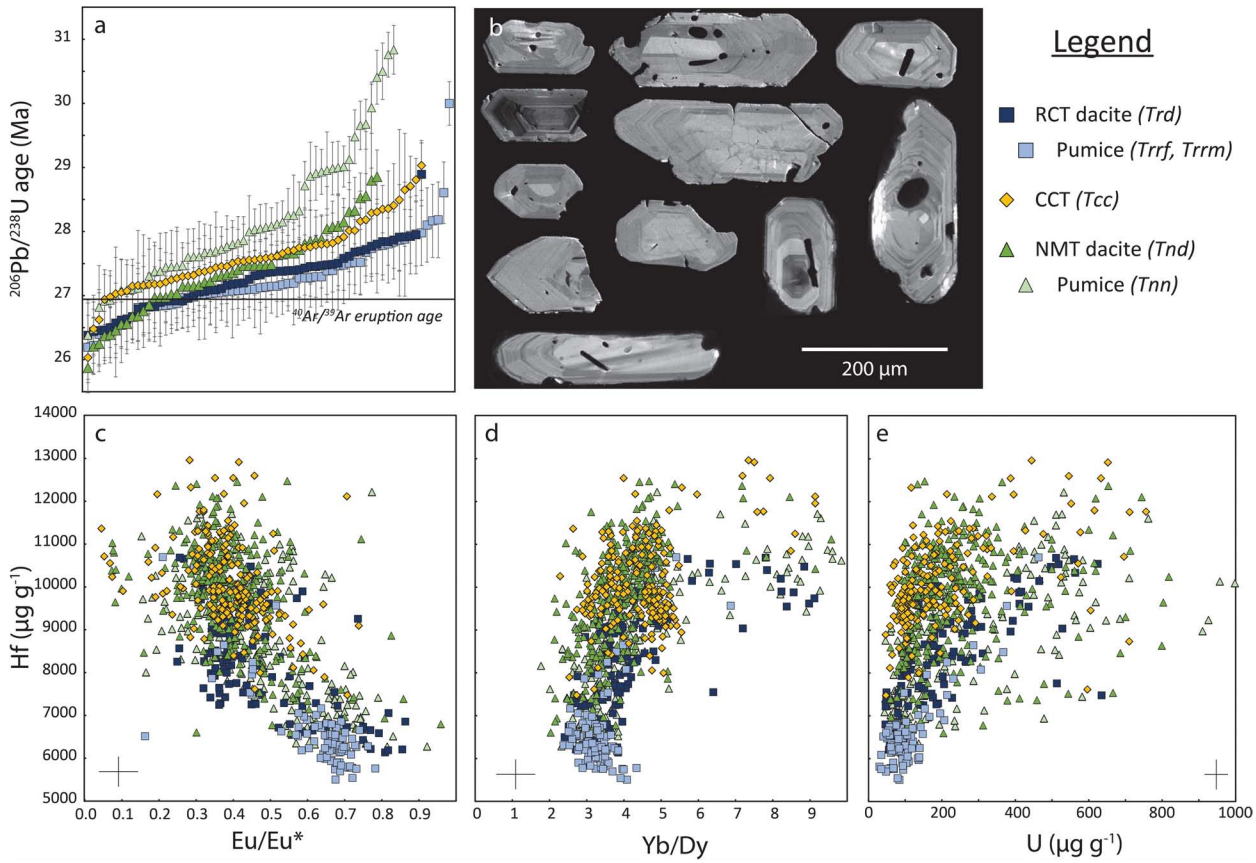

FIGURE 6 | Zircon U-Pb ages and trace element chemistry. **(a)** U-Pb ages of representative samples from the NMT, CCT, and RCT (including "mafic" and "felsic" pumices, showing pronounced old age tail for the NMT rhyolitic pumice [ages corrected for alpha radiation dose and Th disequilibrium; $^{40}Ar/^{39}Ar$ eruption age = 26.9 Ma; (Lipman and McIntosh, 2008)]. **(b)** CL images of zircons from the NMT, showing diversity in zoning patterns. **(c–e)** Eu/Eu*, Yb/Dy, and U vs. Hf (µg g^{-1}), demonstrating increased Eu/Eu* for RCT pumices, correlated with decreased Yb/Dy (indicating absence of titanite), U and Hf (indicating increased crystallization temperature). Error bars show conservative ~5% 2s uncertainty.

It should be noted that while the sum of these observations suggests such an interpretation, the temperatures provided must be interpreted with caution due to complications in applying the geothermometer of Ferry and Watson (2007). In particular, we assume constant values for a_{TiO2} and a_{SiO2}, and do not consider variations in a_{TiO2} and a_{SiO2} resulting from variability in temperature and crystallizing mineral assemblage because of the inherent uncertainty in predicting their values throughout the petrogenetic sequence. Furthermore, we do not separate analyses from different sectors within the zircons, which have well-documented variations in Ti and other trace elements (Chamberlain et al., 2014). We posit that this is unlikely to affect the interpretations for three reasons: (1) strong sector zoning similar to the Bishop Tuff is rarely observed in our samples; (2) the majority of analytical spots are selected at the tips of the zircons because of the larger available surface area; finally, (3) while (Chamberlain et al., 2014) demonstrated an enrichment in both Ti and Hf in zircon tips, these two elements are commonly observed to *inversely* correlate in zircon suites, including this study (**Supplementary Figure S7**), suggesting that increased Ti results does not result from preferential analysis of zircon tips. Hafnium concentrations in zircon increase with degree of fractionation [and in general, temperature; see Claiborne et al. (2006), Cooper et al. (2014)], but the development of a Hf-in-zircon thermometer is hindered by the fact that a_{Hf2O}, unlike a_{TiO2}, is unconstrained in magmatic systems (Watson et al., 2006). Regardless, the decreased Hf concentrations in RCT pumice zircons is consistent with a hotter/more depolymerized melt, as is the increased Ti concentration. While temperature estimates may be improved by a more rigorous targeting of tips, it is unlikely that such a study would change the interpretation. As there are inherent uncertainties in the Ti-in-zircon thermometer, compounded by the simplified assumptions of a_{TiO2} and a_{SiO2} in this study, we suggest that our temperature estimates be interpreted in a semi-quantitative manner, as they may reflect variations larger or smaller than their true values (see also **Supplementary Figure S9**).

Similarity of the Rat Creek and Nelson Mountain Tuffs

The close temporal and spatial correlations of the RCT and NMT have long been suggestive of a shared magmatic history

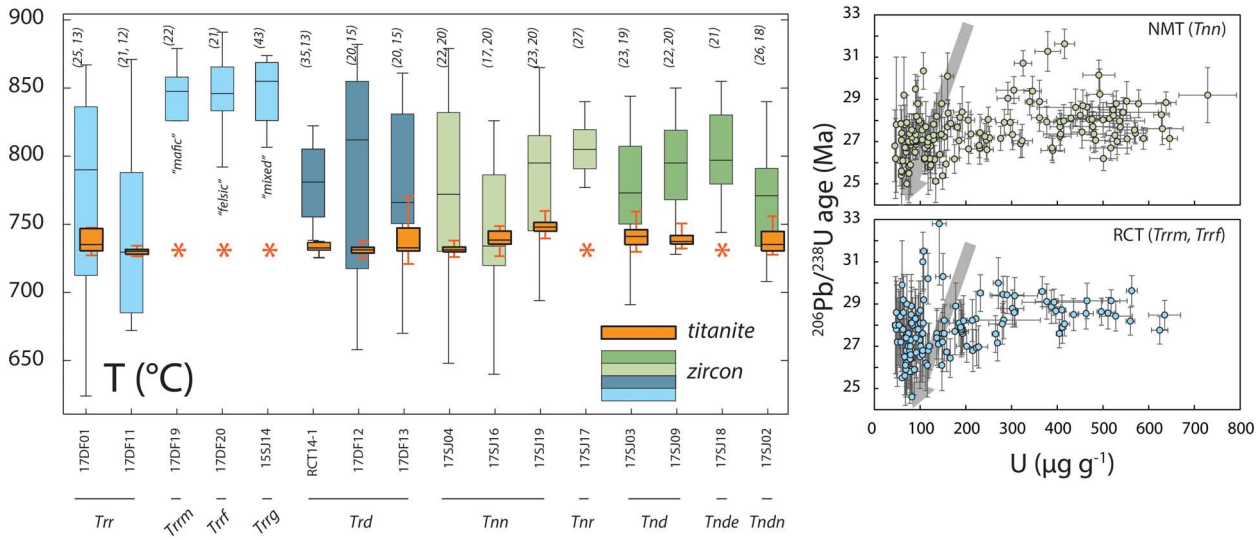

FIGURE 7 | Left: crystallization temperatures of zircon and titanite using the Ti-in-zircon (Ferry and Watson, 2007) and Zr-in-titanite (Hayden et al., 2008) geothermometers (stars denote lack of titanite). **Right:** $^{206}Pb/^{238}U$ ages of zircons from the pumiceous NMT **(top)** and RCT **(bottom)**, demonstrating a decrease in age for the low-U sub-population (gray arrows). Error bars show 2 s uncertainty. Boxes represent median and 1st/3rd quartiles; whiskers represent the 10th and 90th percentiles; numbers in parentheses indicate number of zircon and titanite analyses, respectively.

together with the CCT (Lipman and McIntosh, 2008), though the heterogeneity within each of the pair has precluded a definitive correlation. Furthermore, the eruption of the CCT between the two units (with the three co-occurring at the Wheeler Geological Monument) provides a compelling rationale for the group representing separate magma reservoirs evolving independently, and therefore necessitates a closer look at the crystal cargo, geochronology and possible magma dynamics to group them together.

The SRMVF can be seen as a crustal section resulting from protracted assimilation-fractional crystallization (AFC)-type differentiation in a long-lived thermal anomaly within the crust (Lipman and Bachmann, 2015), akin to other magmatic arcs such as the Sesia-Ivrea zone (Swiss/Italian Alps; Karakas et al., 2019), Kohistan Arc (NW Pakistan; Jagoutz et al., 2009), and Famatinian Arc (western Argentina; Walker et al., 2015). Viewed in this context, with magmas in an integrated magma system gradually becoming more silicic upward, the zoned ignimbrites of the SRMVF (RCT, NMT, and CRT) seem to represent a microcosm of the crustal distillation process, and contain a corresponding diversity in mineral compositions.

Feldspar chemistry, for example, shows wide variability in An and Or content (An_{20-45} for plagioclase and Or_{55-75} for sanidine) within both units, which essentially captures the entire variability in the SRMVF (Lipman and Weston, 2001), and shows a similar amount of diversity as other large zoned ignimbrites [e.g., Szymanowski et al. (2019)] caused by variations in crystallization temperature, pressure and a_{H2O}. This is corroborated with amphibole chemistry in the RCT and NMT, with variability in Al_2O_3 content indicative of diverse crystallization pressures. Clinopyroxene major element chemistry is relatively consistent between all units, apart from rhyolitic pyroxenes which demonstrate concurrent increases in Eu/Eu* and decreases in total REE concentration consistent with crystallization from an evolving magma reservoir (**Supplementary Figure S5**). Given the diversity in mineral compositions, it is perhaps more informative to look at glass compositions when correlating the units. Excluding the "mafic" pumice glass (discussed above), the trace element concentrations of the RCT and NMT glasses are consistent with one another (**Figure 2**), indicating either a shared magmatic history or a very similar time-temperature-compositional path (not mutually exclusive). Given that such large magmatic reservoirs often contain physically separated melt lenses [e.g., Gravley et al. (2007), Ellis et al. (2014), Wotzlaw et al. (2014), Szymanowski et al. (2019)], it is clear that small variations in glass trace element concentrations will occur.

Biotite trace element chemistry is more complex, given the mineral's crystallization over a wide range of compositions and its partitioning of an array of trace elements. It has been used for geochemical fingerprinting in Toba (Smith et al., 2011), New Zealand (Shane et al., 2003), as well as Tenerife, where the incorporation of elements with bulk D∼1 (V, Co, Nb, and Mn) is particularly informative (Sliwinski et al., 2017b). While the production of small magma batches on short ($\sim 10^4$ yr) timescales in Tenerife may generate trace element compositions that vary drastically depending on the composition of a parent melt, magmatic systems in the SRMVF are sufficiently long-lived (Wotzlaw et al., 2013), spatially extensive (Lipman et al., 1997) and prone to homogenization (Bachmann et al., 2002; Huber et al., 2011) that their major and trace element chemistry remains relatively constant over time. This being the case, fingerprinting eruptions becomes more difficult, and variations in trace elements are more likely to reflect magmatic processes

than distinct geochemical signatures. For example, Mn in biotite increase with degree of fractionation owing to the bulk incompatibility of Mn (Watson, 1977; Hirschmann and Ghiorso, 1994), while elements like Co and V decrease as they are scavenged by Fe-Ti oxides (**Figure 4c**). Both the RCT and NMT contain high-Mn, low-V, Co biotites in their rhyolitic subunits, indicative of high degrees of fractionation, in addition to low-Mn, high-V and -Co biotites in their dacitic subunits that essentially overlap with other SRMVF units. Additionally, the rhyolitic subunits feature a unique group of low-Mn, low-V, Co biotites (**Figures 4a,d**), with high Ba indicative of magmatic rejuvenation (doped with cumulate feldspar melt).

Just as compositional parameters do not reveal any significant differences between the RCT and NMT, zircon age spectra do not separate the units and instead show consistent behavior with ages at or slightly above the $^{40}Ar/^{39}Ar$ eruption age (**Figure 6a** and **Supplementary Figure S8**), and also consistent with CCT ages. Here, a few points should be noted: (1) the systematic uncertainties which provide the largest source of error in LA-ICP-MS U-Pb ages (Horstwood et al., 2016) were minimized by analyzing all samples in the same session in a randomized order, leading to maximum confidence in the distribution of ages; (2) the weighted mean zircon ages are inconsistent with the stratigraphic order of the complex, with stratigraphically oldest RCT zircons demonstrating the youngest ages in the complex (both before and after alpha dose correction). This highlights the fact that zircons may experience protracted crystallization prior to eruption, and also makes it unlikely that the use of high-precision methods will go further in differentiating these units. Finally, one should note that the old rhyolitic NMT ages are the result of a pronounced but difficult to constrain age tail, which is likely the result of assimilation of zircons from previous SRMVF eruptions or the analysis of small xenocrystic Proterozoic cores. This unit contains a number of 1,400–1,600 Ma zircon xenocrysts which fit the dominant age of the Proterozoic basement rocks, and it is likely that the analysis of a dominantly Cenozoic zircon with the slightest addition of a xenocryst would yield a slightly older, yet still concordant age. For this reason, no attempt at constraining magma evolution times is presented.

Nevertheless, shared zircon age distributions suggest a shared magmatic origin for the RCT and NMT, along with broad similarity in mineral compositions. The close timing in $^{40}Ar/^{39}Ar$ eruption age as well as coincidence in location seem to corroborate this, but the overlapping San Luis calderas raise an important question: How does one explain the eruption of a zoned ignimbrite followed by a chemically distinct mafic dacite (CCT), and then the same zoned ignimbrite out of the same caldera complex?

Magma Reservoir Geometry and Magmatic Flux Considerations

In addition to the spatially coincident calderas of the San Luis Complex, there lies in the northeast the Cochetopa caldera, with a large spatial extent (~20 × 25 km) seemingly inconsistent with the limited caldera infill (see Introduction). The subsidence of this caldera shortly prior to the eruption of the NMT (inferred from the ponding of NMT within the structure and the Cochetopa Graben that connects it to the other San Luis calderas) has been interpreted as evidence that it overlies the source of the NMT magma (Lipman and McIntosh, 2008). This would necessitate lateral magma migration from the NE, but at a scale not previously observed (100's of km^3 vs. 10's of km^3 in previous studies). The proposed model for the eruption of this complex system is outlined below.

The San Luis magmas are the apical part of a laterally- and vertically extensive integrated magma reservoir (Hildreth and Moorbath, 1988), which due to thermal buffering by a crustal thermal anomaly (Karakas et al., 2017), and latent heat of crystallization (Gelman et al., 2013), persists for an extended amount of time (Wotzlaw et al., 2013) within a "mushy," easily eruptible state (Bachmann and Bergantz, 2003). In particular, the rhyolitic RCT represents the most evolved magmatic compositions in a magma reservoir with a geometry that extends from the present-day San Luis caldera complex to the northeast underlying Cochetopa Park (**Figure 1**). The rejuvenation of this system with mafic recharge [akin to the CRT, see Bachmann et al. (2014)] allows for the mobilization of dacitic RCT magma, with the resultant thermal and compositional effects visible in biotite, zircon, and to a lesser extent feldspar, compositions (**Figure 8A**). The eruption of the RCT disturbs the magma reservoir, allowing for the mobilization of CCT magma (the typical non-cumulate mush in the area, akin to the Fish Canyon Tuff, or Snowshoe Mountain Tuff; **Figure 8B**), while the caldera collapse associated with the RCT precludes further eruption from that region of the magma reservoir. Following the eruption of the CCT atop the RCT (**Figure 8C**), the remainder of the mobile magma beneath Cochetopa Park migrates laterally to the SW and erupts (**Figure 8D**), generating two additional caldera collapse structures in the San Luis complex and in Cochetopa park (**Figure 8E**). During this stage, the Los Pinos Graben, which connects the two reservoirs, is partly infilled by the NMT (**Figure 1**). In this model, it should be noted that we draw a strong distinction between magma extraction (i.e., crystal-melt segregation to create low-crystallinity rhyolites) and magma assembly. While the former process occurs over long timescales to produce melt-rich magmas, the latter can be comparatively rapid (decades to centuries), tapping pre-existing melt batches to create larger eruptions (e.g., Druitt et al., 2012) through processes akin to the lateral magma migration inferred here.

The phenomenon of lateral magma migration has been previously documented [e.g., Katmai, Hildreth (1991); Taupo Volcanic Zone, Gravley et al. (2007), Cooper et al. (2012); Kirishima, Brothelande et al. (2018)], as has the rapid assembly of melt-dominant magma batches [e.g., during the Rocky Hill eruption; see Cooper et al. (2017)]. These phenomena are integral when considered in the context of calculating magmatic fluxes. A common contention in the field of magmatic petrology is that the rate of magma transport (in km^3/yr) dictates the behavior of the system, such that low fluxes lead to solidification of magma and production of plutons, while high fluxes lead to the generation of ignimbrites (Coleman et al., 2004; Glazner et al., 2004; Mills and Coleman, 2013; Caricchi et al., 2014; Gaynor et al., 2019a). In this model, the high fluxes necessary for the

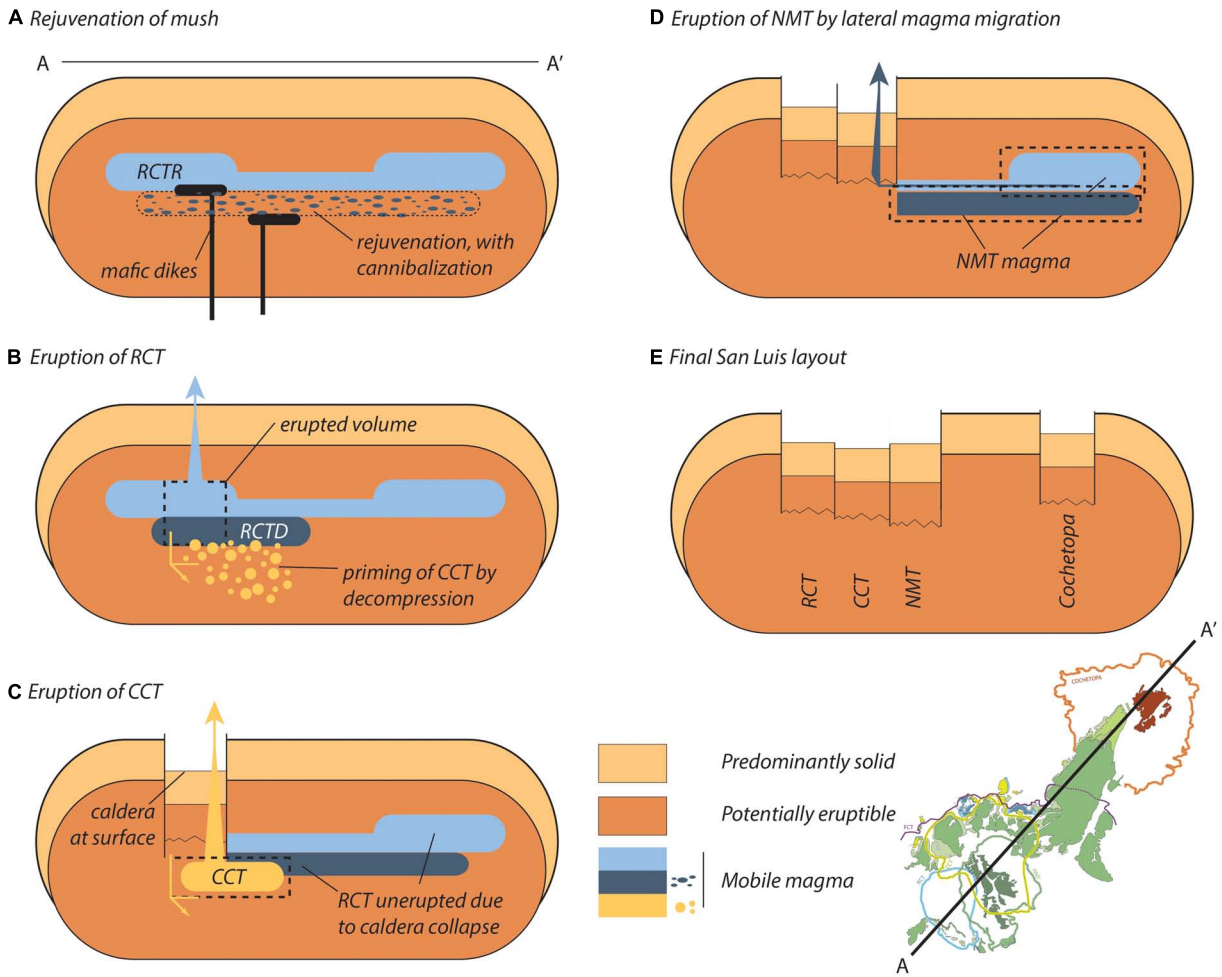

FIGURE 8 | Proposed model for the eruption of the San Luis ignimbrites, represented as a cross-section through the geological map in **Figure 1** (see inset): **(A)** a laterally extensive zoned (rhyolite-dacite) magma body is the predecessor of the RCT and NMT. Rejuvenation by mafic recharge mobilizes mushy magma, giving rise to the dacitic subunit of both. **(B)** Eruption of the RCT liberates part of the magma body, with the remainder of the eruption curtailed by caldera collapse. At this stage, CCT magma is likely mobilized from adjacent mush (represented by yellow spots). **(C)** The CCT erupts. **(D)** The remainder of the RCT/NMT magma migrates southwest from Cochetopa Park and erupts from the same area as the CCT and RCT, leading to caldera collapse structures in both the San Luis complex and in Cochetopa Park **(E)**. Horizontal and vertical scales are schematically represented.

creation of large-volume ignimbrites necessitate the sourcing of high volumes of silicic magma from a lower-crustal hot zone (Annen, 2009), as opposed to the storage and fractionation of silicic magma in upper-crustal magma chambers (Bachmann and Bergantz, 2004). The different characteristic fluxes of plutons and ignimbrites seem to suggest that a fundamentally different process contributes to the generation of each, but we contend that all silicic magmas are produced by the same, predominantly AFC-driven, process. A thought experiment is provided below to demonstrate that a separate process for large-volume ignimbrites is not necessary.

In nearly all scientific fields, the term "flux" refers not to unit volume per unit time (e.g., $km^3\ yr^{-1}$), but to volume per time *per unit area*, which results in units of distance over time, or velocity. The velocity of magma through the crust is essentially dependent on its viscosity, which in turn depends on temperature: magma viscosity increases exponentially as its temperature drops, and the effective velocity goes to 0 as the magma crystallizes. Therefore, the temperature (i.e., the size of the crustal thermal anomaly) effectively controls the magmatic flux of a system. This means that a large volcanic field representing a large crustal thermal anomaly (e.g., the SRMVF or the APVC) will indeed have a larger magmatic flux than a smaller field of similar geometry [e.g., the Pannonian Basin, see Lukács et al. (2015)]. However, this flux should be calculated as $km^3\ kyr^{-1}\ km^{-2}$ by normalizing to the footprint of the magmatic units, if one wishes to differentiate between an unusually fast rate of magma assembly and an unusually high crustal heat flow. This way, increased magmatic flux can be attributed directly to increased average magma ascent velocity (higher thermal anomaly) without invoking further petrogenetic processes. As discussed below, this method provides very consistent estimates compared to volume/time flux (km^3

kyr^{-1}), and illustrates that previously reported "high magma fluxes" are in fact a mathematical artifact.

For instance, if the RCT and NMT were separate magmas of 150 and 500 km^3 volume (respectively), and each evolved over ∼450 ka [the time since the eruption of the Wason Park Tuff at 27.35 Ma; Lipman and McIntosh (2008)], then the two have volume/time fluxes of ∼0.3 and ∼1.1 km^3 kyr^{-1}. If one assumes that they represent a single magma body, as suggested by this study, this suddenly becomes ∼1.4 km^3 kyr^{-1}, thereby increasing the estimated rate of a physical process (e.g., the rate of crystal-melt segregation) simply by changing the accounting procedure. By contrast, normalizing the volume/time flux with the caldera area provides consistent results: the RCT has a poorly constrained caldera geometry of ∼9 × 12 km, while the NMT has two calderas: a smaller 9 × 9 km caldera in the San Luis as well as a 20 × 25 km caldera at Cochetopa Park. The areas of these three calderas, assuming simple ellipsoidal geometry, amount to 85, 64 and 393 km^2, respectively, totaling 85 km^2 for the RCT and 457 km^2 for the NMT (531 km^2 if one also counts the area of the ∼5 × 15 km Cochetopa Graben). Assuming again a timescale of 450 kyr, the RCT has a flux of 3.9×10^{-3} km^3 kyr^{-1} km^{-2}, while the NMT has a flux of 2.1×10^{-3} km^3 kyr^{-1} km^{-2} (**Table 2**). Considering the two as one system yields a flux of 3.0×10^{-2} km^3 kyr^{-1} km^{-2}, which is simply the average of the two fluxes and consistent with established mathematic practices of calculating total flux.

Applying the same logic to other ignimbrites in the SRMVF (e.g., the FCT and CRT) yields consistent upper crustal magma flux estimates between 2.1 and 5.5×10^{-3} km^3 kyr^{-1} km^{-2}, similar to plutonic units. The Mount Princeton Batholith in the northern SRMVF yields an estimate of 2.4×10^{-3} using area estimates and vertical exposure (for a cylindrical geometry) in addition to ID-TIMS zircon ages from Mills and Coleman (2013). Meanwhile, estimates from the nearby Questa-Latir region [recently compiled by Gaynor et al. (2019a), including data from Tappa et al. (2011), Gaynor et al. (2019b), and Rosera et al. (2013)] yield estimates of 0.8 to 4.1×10^{-3} km^3 kyr^{-1} km^{-2} (**Table 2**). On average, plutonic units have fluxes of 3.2×10^{-3} km^3 kyr^{-1} km^{-2} compared with 3.8×10^{-3} km^3 kyr^{-1} km^{-2} for volcanic units mentioned above, consistent with the hypothesis of cogenetic origin. However, one should refrain from quoting these numerical estimates for a number of reasons: (1) age spans vary between studies and with the amount of zircons sampled. For example, we chose an age span of 440 ka for the FCT based on the high-precision ages provided by Wotzlaw et al. (2013). Using the longer timescale (600 ka) of Bachmann et al. (2007) would decrease the apparent flux, but there is no good justification for favoring one study over the other. (2) Both volcanic and plutonic volumes are difficult to estimate. Plutonic volumes are difficult because there is no caldera structure to suggest the original volume of magma – there is only what remains exposed at the surface. Meanwhile, volcanic volumes are difficult because of their widespread and often heterogeneous coverage of the landscape, along with the fact that the erupted volumes likely underestimate the amount of eruptible magma available. Finally, the estimates of caldera area used to estimate the original magmatic footprint and the volume of caldera infill rely on the topographic margin of the caldera rather than the hidden structural margin, thereby yielding a slight overestimate. However, even with the error associated with these estimates, the flux estimates are comparable, and far from the order-of-magnitude difference between plutonic and volcanic units reported by other authors (Annen, 2009; Mills and Coleman, 2013; Gaynor et al., 2019a).

TABLE 2 | Calculated magma fluxes from SRMVF ignimbrites and plutons.

Unit	Width [km]	Length [km]	Area [km^2]	Volume [km^3]	Age Span [kyr]	Flux [km^3 kyr^{-1} km^{-2}]	Age source*
San Juan locus							
Nelson Mountain**	20 (9)	25 (9)	531**	500	450	2.1×10^{3}	*Time since WPT eruption*
Cebolla creek	14	16	176	300	450	3.8×10^{-3}	*Time since WPT eruption*
Rat Creek	9	12	85	150	450	3.9×10^{-3}	*Time since WPT eruption*
Carpenter ridge	25	30	589	1000	470	3.6×10^{-3}	*Time since FCT eruption*
Fish Canyon	35	75	2062	5000	440	5.5×10^{-3}	Wotzlaw et al., 2013
Mount princeton	20	30	450	675	630	2.4×10^{-3}	Mills and Coleman, 2013
Questa-Latir***							
Cabresto lake	8	12	75	60.3	120	6.7×10^{-3}	Tappa et al., 2011
Red river suite	10	10	79	31.4	120	3.3×10^{-3}	Rosera et al., 2013
Questa granite	10	20	157	47.1	380	7.9×10^{-4}	Rosera et al., 2013
Deep granite	10	20	157	62.8	140	2.9×10^{-3}	Gaynor et al., 2019a
Rio hondo	14	22	242	360.9	620	2.4×10^{-3}	Tappa et al., 2011
Lucero peak	10	10	79	62.8	195	4.1×10^{-3}	Gaynor et al., 2019b
Average, ignimbrites						3.8×10^{-3}	
Average, plutons						3.2×10^{-3}	

**Sources in bold derived from maximum and minimum zircon ID-TIMS ages. **NMT has two calderas measuring 20 × 25 and 9 × 9 km. Total area represents the sum of these and the approximate area beneath the ∼rectangular Cochetopa graben measuring ∼5 × 15 km. ***Area and volume estimates compiled by Gaynor et al. (2019a).*

The similarity of volcanic and plutonic fluxes noted here requires three additional points of emphasis. First, the flux estimates pertain to only the *upper* crust in the SRMVF. The bulk of crustal magmatic flux occurs in the lower crust and is not manifested as surface volcanism, contributing instead to the building of continental crust or cumulates (Johnson, 1991; De Silva and Gosnold, 2007; Jagoutz and Schmidt, 2013). Second, while it is possible that other magmatic provinces are characterized by higher or lower magma flux, it is crucial to compare plutons, and volcanics from *the same magmatic province* in order to discern between an anomaly in evolutionary processes and an anomaly in crustal heat flux. That is, while slow plutonic assembly can be demonstrated in some regions (e.g., the Tuolumne Instrusive Suite; see Coleman et al., 2004), these rates are not easily comparable to ignimbrites in the SRMVF, and one should not derive from this the conclusion that large-volume ignimbrites are formed by a fundamentally different process from their underlying batholiths. This is, however, enough to suggest a difference in upper crustal magmatic flux between the two regions, which is a function of the crustal thermal regime. Finally, the phenomenon of lateral magma migration may be critical to resolving the debate about the rates of silicic magma generation. While the close timing of the CCT and NMT previously suggested rapid magma generation, the sourcing of the NMT from afar suggests that it had evolved long before, and not shortly after the eruption of its predecessor.

CONCLUSION

The similarity of the Nelson Mountain and Rat Creek Tuffs in appearance, mineralogy, and spatial extent have long made their distinction difficult, and this is compounded by their identical $^{40}Ar/^{39}Ar$ eruption ages (Lipman and McIntosh, 2008). The stratigraphic appearance of the Cebolla Creek Tuff between the two units has been the most robust argument for their separation, but we present an alternative model to argue for their shared magmatic origin and discuss the implications on magma flux estimations. In particular:

1. The degree of zoning in both units is accompanied by exceptional diversity in biotite, feldspar, pyroxene, amphibole, glass and zircon compositions, indicating a protracted history of polybaric differentiation for both units.
2. The appearance of distinct high-temperature biotite and zircon populations preserved in pumices within both units suggests intense reheating and rejuvenation prior to eruption, consistent with the young U-Pb ages recorded by zircons.
3. The seemingly anomalous appearance of the chemically distinct Cebolla Creek Tuff between the two units can be reconciled by considering a model whereby the NMT and RCT are stored in a laterally extensive magma reservoir that erupts in two phases, before and after the CCT. This is supported by the formation of the nearby Cochetopa Caldera during the eruption of the NMT and can be used to demonstrate that the production of silicic magmas need not be rapid as postulated by some (Lipman and McIntosh, 2008).
4. Considering the NMT and RCT as one unit adjusts the magmatic flux estimate (i.e., the eruptible magma production rate) in a way that demonstrates the shortcomings of relying on volume/time flux calculations: summing them apparently increases the volumetric flux without taking into account the increase in the system's areal footprint. Accordingly, an alternate method is proposed whereby volume/time estimates are normalized to the footprint of a magma system leading to flux units of $km^3\ kyr^{-1}\ km^{-2}$. Such treatment generates magmatic flux estimates that are consistent between volcanic units, and also consistent with ∼cogenetic plutonic units, as would be expected from magmas that are generated by the same physical processes.

DATA AVAILABILITY STATEMENT

All datasets generated for this study are included in the manuscript/**Supplementary Files**.

AUTHOR CONTRIBUTIONS

JS and OB conceived the study. JS, DF, OB, and PL performed the fieldwork. JS, DF, and MG collected the data. JS wrote the manuscript with the help of OB, PL, and DF. All authors contributed to the interpretation and evaluation of data.

FUNDING

This study was supported by the ETH Research Grant ETH-34 15-2 (JS).

ACKNOWLEDGMENTS

We would like to express gratitude to Matthew Zimmerer for his assistance and guidance in the field, as well as Chad Deering for help in obtaining sample material. Assistance in the laboratory from Alina Fiedrich, Gabriela Ligęza, and Calvin Kuntze was greatly appreciated.

SUPPLEMENTARY MATERIAL

The Supplementary Material for this article can be found online at: https://www.frontiersin.org/articles/10.3389/feart.2019.00271/full#supplementary-material

REFERENCES

Allan, A. S., Morgan, D. J., Wlson, C. J., and Millet, M.-A. (2013). From mush to eruption in centuries: assembly of the super-sized Oruanui magma body. *Contrib. Mineral. Petrol.* 166, 143–164. doi: 10.1007/s00410-013-0869-2

Allaz, J. M., Popa, R. G., Reusser, E., and Martin, L. (2019). Electron microprobe analysis of minor and trace elements in beam sensitive materials: how far can we go? *Microsc. Microanal.* 25, 2312–2313. doi: 10.1017/s1431927619012297

Anderson, J. L., and Smith, D. R. (1995). The effects of temperature and f O2 on the Al-in-hornblende barometer. *Am. Mineral.* 80, 549–559. doi: 10.2138/am-1995-5-614

Annen, C. (2009). From plutons to magma chambers: thermal constraints on the accumulation of eruptible silicic magma in the upper crust. *Earth Planet Sci. Lett.* 284, 409–416. doi: 10.1016/j.epsl.2009.05.006

Bachmann, O., and Bergantz, G. W. (2003). Rejuvenation of the fish canyon magma body: a window into the evolution of large-volume silicic magma systems. *Geology* 31, 789–792.

Bachmann, O., and Bergantz, G. W. (2004). On the origin of crystal-poor rhyolites: extracted from batholithic crystal mushes. *J. Petrol.* 45, 1565–1582. doi: 10.1093/petrology/egh019

Bachmann, O., Deering, C. D., Lipman, P. W., and Plummer, C. (2014). Building zoned ignimbrites by recycling silicic cumulates: insight from the 1,000 km3 carpenter ridge tuff, CO. *Contrib. Mineral. Petrol.* 167: 1025.

Bachmann, O., and Dungan, M. A. (2002). Temperature-induced Al-zoning in hornblendes of the Fish Canyon magma. *Colo. Am. Mineral.* 87, 1062–1076. doi: 10.2138/am-2002-8-903

Bachmann, O., Dungan, M. A., and Lipman, P. W. (2002). The fish canyon magma body, San Juan volcanic field, colorado: rejuvenation and eruption of an upper-crustal batholith. *J. Petrol.* 43, 1469–1503. doi: 10.1093/petrology/43.8.1469

Bachmann, O., and Huber, C. (2016). Silicic magma reservoirs in the Earth's crust. *Am. Mineral.* 101, 2377–2404. doi: 10.2138/am-2016-5675

Bachmann, O., and Huber, C. (2018). The inner workings of crustal distillation columns; the physical mechanisms and rates controlling phase separation in silicic magma reservoirs. *J. Petrol.* 60, 3–18. doi: 10.1093/petrology/egy103

Bachmann, O., Oberli, F., Dungan, M. A., Meier, M., Mundil, R., and Fischer, H. (2007). Ar-40/Ar-39 and U-Pb dating of the fish canyon magmatic system, San Juan Volcanic field, colorado: evidence for an extended crystallization history. *Chem. Geol.* 236, 134–166. doi: 10.1016/j.chemgeo.2006.09.005

Barboni, M., Annen, C., and Schoene, B. (2015). Evaluating the construction and evolution of upper crustal magma reservoirs with coupled U/Pb zircon geochronology and thermal modeling: a case study from the Mt. capanne pluton (Elba, Italy). *Earth Planet. Sci. Lett.* 432, 436–448. doi: 10.1016/j.epsl.2015.09.043

Black, L. P., Kamo, S. L., Allen, C. M., Davis, D. W., Aleinikoff, J. N., and Valley, J. W. (2004). Improved 206 Pb/238 U microprobe geochronology by the monitoring of a trace-element-related matrix effect; SHRIMP, ID–TIMS, ELA–ICP–MS and oxygen isotope documentation for a series of zircon standards. *Chem. Geol.* 205, 115–140. doi: 10.1016/j.chemgeo.2004.01.003

Blundy, J. D., and Holland, T. J. (1990). Calcic amphibole equilibria and a new amphibole-plagioclase geothermometer. *Contrib. Mineral. Petrol.* 104, 208–224. doi: 10.1007/bf00306444

Brothelande, E., Amelung, F., Yunjun, Z., and Wdowinski, S. (2018). Geodetic evidence for interconnectivity between Aira and Kirishima magmatic systems, Japan. *Sci. Rep.* 8:9811. doi: 10.1038/s41598-018-28026-4

Caricchi, L., Simpson, G., and Schaltegger, U. (2014). Zircons reveal magma fluxes in the Earth's crust. *Nature* 511, 457–461. doi: 10.1038/nature13532

Chamberlain, K. J., Morgan, D. J., and Wilson, C. J. N. (2014). Timescales of mixing and mobilisation in the Bishop Tuff magma body: perspectives from diffusion chronometry. *Contrib. Mineral. Petrol.* 168:1034.

Claiborne, L. L., Miller, C., Walker, B., Wooden, J., Mazdab, F., and Bea, F. (2006). Tracking magmatic processes through Zr/Hf ratios in rocks and Hf and Ti zoning in zircons: an example from the Spirit Mountain batholith, Nevada. *Mineral. Mag.* 70, 517–543. doi: 10.1180/0026461067050348

Coleman, D. S., Gray, W., and Glazner, A. F. (2004). Rethinking the emplacement and evolution of zoned plutons: geochronologic evidence for incremental assembly of the Tuolumne Intrusive Suite, California. *Geology* 32, 433–436.

Cooper, G. F., Morgan, D. J., and Wilson, C. J. (2017). Rapid assembly and rejuvenation of a large silicic magmatic system: INsights from mineral diffusive profiles in the Kidnappers and Rocky Hill deposits, New Zealand. *Earth Planet. Sci. Lett.* 473, 1–13. doi: 10.1016/j.epsl.2017.05.036

Cooper, G. F., Wilson, C. J., Charlier, B. L., Wooden, J. L., and Ireland, T. R. (2014). Temporal evolution and compositional signatures of two supervolcanic systems recorded in zircons from Mangakino volcanic centre, New Zealand. *Contrib. Mineral. Petrol.* 167:1018.

Cooper, G. F., Wilson, C. J., Millet, M.-A., Baker, J. A., and Smith, E. G. (2012). Systematic tapping of independent magma chambers during the 1 Ma Kidnappers supereruption. *Earth Planet. Sci. Lett.* 313, 23–33. doi: 10.1016/j.epsl.2011.11.006

Cooper, K. M., and Kent, A. J. R. (2014). Rapid remobilization of magmatic crystals kept in cold storage. *Nature* 506, 480–483. doi: 10.1038/nature12991

Curtis, G. H. (1968). "The stratigraphy of the ejecta from the 1912 eruption of mount katmai and novarupta, alaska," in *Studies in Volcanology*, eds R. R. Coats, R. L. Hay, and C. A. Anderson, (Boulder, CO: Geological Society of America).

De Silva, S. L., and Gosnold, W. D. (2007). Episodic construction of batholiths: insights from the spatiotemporal development of an ignimbrite flare-up. *J. Volcanol. Geothermal Res.* 167, 320–335. doi: 10.1016/j.jvolgeores.2007.07.015

Deering, C., and Bachmann, O. (2010). Trace element indicators of crystal accumulation in silicic igneous rocks. *Earth Planet. Sci. Lett.* 297, 324–331. doi: 10.1016/j.epsl.2010.06.034

Deering, C., Bachmann, O., and Vogel, T. (2011). The ammonia tanks tuff: erupting a melt-rich rhyolite cap and its remobilized crystal cumulate. *Earth Planet. Sci. Lett.* 310, 518–525. doi: 10.1016/j.epsl.2011.08.032

Degruyter, W., Huber, C., Bachmann, O., Cooper, K. M., and Kent, A. J. (2016). Magma reservoir response to transient recharge events: the case of Santorini volcano (Greece). *Geology* 44, 23–26. doi: 10.1130/g37333.1

Druitt, T. H., Costa, F., Deloule, E., Dungan, M., and Scaillet, B. (2012). Decadal to monthly timescales of magma transfer and reservoir growth at a caldera volcano. *Nature* 482, 77–80. doi: 10.1038/nature10706

Dufek, J., and Bachmann, O. (2010). Quantum magmatism: magmatic compositional gaps generated by melt-crystal dynamics. *Geology* 38, 687–690. doi: 10.1130/g30831.1

Ellis, B. S., Bachmann, O., and Wolff, J. A. (2014). Cumulate fragments in silicic ignimbrites: the case of the Snake River Plain. *Geology* 42, 431–434. doi: 10.1130/g35399.1

Erdmann, S., Martel, C., Pichavant, M., and Kushnir, A. (2014). Amphibole as an archivist of magmatic crystallization conditions: problems, potential, and implications for inferring magma storage prior to the paroxysmal 2010 eruption of Mount Merapi, Indonesia. *Contrib. Mineral. Petrol.* 167, 1016.

Evans, B. W., and Bachmann, O. (2013). Implications of equilibrium and disequilibrium among crystal phases in the Bishop Tuff. *Am. Mineral.* 98, 271–274. doi: 10.2138/am.2013.4280

Ferry, J., and Watson, E. (2007). New thermodynamic models and revised calibrations for the Ti-in-zircon and Zr-in-rutile thermometers. *Contrib. Mineral. Petrol.* 154, 429–437. doi: 10.1007/s00410-007-0201-0

Flaherty, T., Druitt, T., Tuffen, H., Higgins, M. D., Costa, F., and Cadoux, A. (2018). Multiple timescale constraints for high-flux magma chamber assembly prior to the Late Bronze age eruption of Santorini (Greece). *Contrib. Mineral. Petrol.* 173:75.

Flinders, A. F., and Shen, Y. (2017). Seismic evidence for a possible deep crustal hot zone beneath Southwest Washington. *Sci. Rep.* 7:7400. doi: 10.1038/s41598-017-07123-w

Forni, F., Degruyter, W., Bachmann, O., De Astis, G., and Mollo, S. (2018a). Long-term magmatic evolution reveals the beginning of a new caldera cycle at Campi Flegrei. *Sci. Adv.* 4:eaat9401. doi: 10.1126/sciadv.aat9401

Forni, F., Petricca, E., Bachmann, O., Mollo, S., De Astis, G., and Piochi, M. (2018b). The role of magma mixing/mingling and cumulate melting in the Neapolitan Yellow Tuff caldera-forming eruption (Campi Flegrei, Southern Italy). *Contrib. Mineral. Petrol.* 173:45.

Forni, F., Ellis, B. S., Bachmann, O., Lucchi, F., Tranne, C. A., Agostini, S., et al. (2015). Erupted cumulate fragments in rhyolites from Lipari (Aeolian Islands). *Contrib. Mineral. Petrol.* 170:49.

Gaynor, S. P., Coleman, D. S., Rosera, J. M., and Tappa, M. J. (2019a). Geochronology of a bouguer gravity low. *J. Geophys. Res* 124, 2457–2468. doi: 10.1029/2018jb015923

Gaynor, S. P., Rosera, J. M., and Coleman, D. S. (2019b). Intrusive history of the oligocene questa porphyry molybdenum deposit, New Mexico. *Geosphere* 15, 548–575. doi: 10.1130/ges01675.1

Gelman, S. E., Gutierrez, F. J., and Bachmann, O. (2013). On the longevity of large upper crustal silicic magma reservoirs. *Geology* 41, 759–762. doi: 10.1130/g34241.1

Ghiorso, M. S., and Gualda, G. A. (2013). A method for estimating the activity of titania in magmatic liquids from the compositions of coexisting rhombohedral and cubic iron–titanium oxides. *Contrib. Mineral. Petrol.* 165, 73–81. doi: 10.1007/s00410-012-0792-y

Glazner, A. F., Bartley, J. M., Coleman, D. S., Gray, W., and Taylor, R. Z. (2004). Are plutons assembled over millions of years by amalgamation from small magma chambers? *GSA Today* 14, 4–12.

Gravley, D., Wilson, C., Leonard, G., and Cole, J. (2007). Double trouble: paired ignimbrite eruptions and collateral subsidence in the Taupo Volcanic Zone, New Zealand. *Geol. Soc. Am. Bull.* 119, 18–30. doi: 10.1130/b25924.1

Gutiérrez, F., Payacán, I., Szymanowski, D., Guillong, M., Bachmann, O., and Parada, M. (2018). Lateral magma propagation during the emplacement of La Gloria Pluton, central Chile. *Geology* 46, 1051–1054. doi: 10.1130/g45361.1

Hayden, L. A., Watson, E. B., and Wark, D. A. (2008). A thermobarometer for sphene (titanite). *Contrib. Mineral. Petrol.* 155, 529–540. doi: 10.1007/s00410-007-0256-y

Hildreth, W. (1991). The timing of caldera collapse at Mount Katmai in response to magma withdrawal toward Novarupta. *Geophys. Res. Lett.* 18, 1541–1544. doi: 10.1029/91gl01083

Hildreth, W. (2004). Volcanological perspectives on Long valley, mammoth mountain, and mono craters: several contiguous but discrete systems. *J. Volcanol. Geothermal Res.* 136, 169–198. doi: 10.1016/j.jvolgeores.2004.05.019

Hildreth, W., and Moorbath, S. (1988). Crustal contributions to arc magmatism in the Andes of central Chile. *Contrib. Mineral. Petrol.* 98, 455–489. doi: 10.1007/bf00372365

Hirschmann, M. M., and Ghiorso, M. S. (1994). Activities of nickel, cobalt, and manganese silicates in magmatic liquids and applications to olivine/liquid and to silicate/metal partitioning. *Geochim. Cosmochim. Acta* 58, 4109–4126. doi: 10.1016/0016-7037(94)90268-2

Holness, M. B., Stock, M. J., and Geist, D. (2019). Magma chambers versus mush zones: constraining the architecture of sub-volcanic plumbing systems from microstructural analysis of crystalline enclaves. *Philos. Trans. R. Soc. A* 377:20180006. doi: 10.1098/rsta.2018.0006

Horstwood, M. S. A., Kosler, J., Gehrels, G., Jackson, S. E., McLean, N. M., Paton, C., et al. (2016). Community-derived standards for LA-ICP-MS U-(Th-)Pb geochronology - uncertainty propagation, age interpretation and data reporting. *Geostand. Geoanal. Res.* 40, 311–332. doi: 10.1111/j.1751-908x.2016.00379.x

Huber, C., Bachmann, O., and Dufek, J. (2011). Thermo-mechanical reactivation of locked crystal mushes: melting-induced internal fracturation and assimilation processes in magmas. *Earth Planet Sci. Lett.* 304, 443–454. doi: 10.1016/j.epsl.2011.02.022

Iwano, H., Orihashi, Y., Hirata, T., Ogasawara, M., Danhara, T., and Horie, K. (2013). An inter-laboratory evaluation of OD-3 zircon for use as a secondary U-Pb dating standard. *Island Arc.* 22, 382–394. doi: 10.1111/iar.12038

Jackson, M., Blundy, J., and Sparks, R. (2018). Chemical differentiation, cold storage and remobilization of magma in the Earth's crust. *Nature* 564, 405. doi: 10.1038/s41586-018-0746-2

Jagoutz, O., and Schmidt, M. W. (2013). The composition of the foundered complement to the continental crust and a re-evaluation of fluxes in arcs. *Earth Planet. Sci. Lett.* 371, 177–190. doi: 10.1016/j.epsl.2013.03.051

Jagoutz, O. E., Burg, J.-P., Hussain, S., Dawood, H., Pettke, T., Iizuka, T., et al. (2009). Construction of the granitoid crust of an island arc part I: geochronological and geochemical constraints from the plutonic Kohistan (NW Pakistan). *Contrib. Mineral. Petrol.* 158:739. doi: 10.1007/s00410-009-0408-3

Jellinek, A. M., and DePaolo, D. J. (2003). A model for the origin of large silicic magma chambers: precursors of caldera-forming eruptions. *Bull. Volcanol.* 65, 363–381. doi: 10.1007/s00445-003-0277-y

Johnson, C. M. (1991). Large−scale crust formation and lithosphere modification beneath Middle to Late Cenozoic calderas and volcanic fields, western North America. *J. Geophys. Res.* 96, 13485–13507. doi: 10.1029/91jb00304

Karakas, O., Degruyter, W., Bachmann, O., and Dufek, J. (2017). Lifetime and size of shallow magma bodies controlled by crustal-scale magmatism. *Nat. Geosci.* 10, 446–450. doi: 10.1038/ngeo2959

Karakas, O., Wotzlaw, J.-F., Guillong, M., Ulmer, P., Brack, P., Economos, R., et al. (2019). The pace of crustal-scale magma accretion and differentiation beneath silicic caldera volcanoes. *Geology* 47, 719–723. doi: 10.1130/g46020.1

Kiss, B., Harangi, S., Ntaflos, T., Mason, P. R., and Pál-Molnár, E. (2014). Amphibole perspective to unravel pre-eruptive processes and conditions in volcanic plumbing systems beneath intermediate arc volcanoes: a case study from Ciomadul volcano (SE Carpathians). *Contrib. Mineral. Petrol.* 167:986.

Lipman, P. (2012). Geologic map of the Cochetopa Park and North Pass calderas, northeastern San Juan Mountains. *Colo.* 312:2.

Lipman, P., Dungan, M., and Bachmann, O. (1997). Comagmatic granophyric granite in the fish canyon tuff, colorado: implications for magma-chamber processes during a large ash-flow eruption. *Geology* 25, 915–918.

Lipman, P. W. (2000). "The central San Juan caldera cluster: regional volcanic framework," in *Ancient Lake Creede: Its Volcano-Tectonic Setting, History of Sedimentation, and Relation of Mineralization in the Creede Mining District*. eds P.M. Bethke, and R.L. Hay, (Boulder, CO: Geological Society of America), 346, 9–69. doi: 10.1130/0-8137-2346-9.9

Lipman, P. W. (2004). *Chemical Analyses of Tertiary Volcanic Rocks, Central San Juan Caldera Complex, Southwestern Colorado*. Reston,VA: US Geological Survey.

Lipman, P. W. (2006). *Geologic Map of the Central San Juan Caldera Cluster, Southwestern Colorado*. Reston,VA: US Geological Survey.

Lipman, P. W., and Bachmann, O. (2015). Ignimbrites to batholiths: Integrating perspectives from geological, geophysical, and geochronological data. *Geosphere* 11, 705–743. doi: 10.1130/ges01091.1

Lipman, P. W., and McIntosh, W. C. (2008). Eruptive and noneruptive calderas, northeastern San Juan Mountains, Colorado: where did the ignimbrites come from? *Geol. Soc. Am. Bull.* 20, 771–795. doi: 10.1130/b26330.1

Lipman, P. W., and Weston, P. E. (2001). *Phenocryst Compositions of Late Ash-Flow Tuffs From the Central San Juan Caldera Cluster: Results From Creede Drill-Hole Samples, and Implications for Regional Stratigraphy*. Reston,VA: US Geological Survey.

Lukács, R., Harangi, S., Bachmann, O., Guillong, M., Danisik, M., Buret, Y., et al. (2015). Zircon geochronology and geochemistry to constrain the youngest eruption events and magma evolution of the Mid-Miocene ignimbrite flare-up in the Pannonian Basin, eastern central Europe. *Contrib. Mineral. Petrol.* 170:52.

Mattinson, J. M. (2005). Zircon U-Pb chemical abrasion ("CA-TIMS") method: combined annealing and multi-step partial dissolution analysis for improved precision and accuracy of zircon ages. *Chem. Geol.* 220, 47–66. doi: 10.1016/j.chemgeo.2005.03.011

Mills, R. D., and Coleman, D. S. (2013). Temporal and chemical connections between plutons and ignimbrites from the Mount Princeton magmatic center. *Contrib. Mineral. Petrol.* 165, 961–980. doi: 10.1007/s00410-012-0843-4

Nandedkar, R. H., Ulmer, P., and Müntener, O. (2014). Fractional crystallization of primitive, hydrous arc magmas: an experimental study at 0.7 *GPa*. *Contrib. Mineral. Petrol.gy* 167, 1015.

Pamukcu, A. S., Carley, T. L., Gualda, G. A., Miller, C. F., and Ferguson, C. A. (2013). The evolution of the peach spring giant magma body: evidence from accessory mineral textures and compositions, bulk pumice and glass geochemistry, and rhyolite-MELTS modeling. *J. Petrol.* 54, 1109–1148. doi: 10.1093/petrology/egt007

Paton, C., Hellstrom, J., Paul, B., Woodhead, J., and Hergt, J. (2011). Iolite: freeware for the visualisation and processing of mass spectrometric data. *J. Anal. At. Spectrom.* 26, 2508–2518.

Petrus, J. A., and Kamber, B. S. (2012). VizualAge: a novel approach to laser ablation ICP-MS U-Pb geochronology data reduction. *Geostand. Geoanal. Res.* 36, 247–270. doi: 10.1111/j.1751-908x.2012.00158.x

Ridolfi, F., Renzulli, A., and Puerini, M. (2010). Stability and chemical equilibrium of amphibole in calc-alkaline magmas: an overview, new thermobarometric formulations and application to subduction-related volcanoes. *Contrib. Mineral. Petrol.* 160, 45–66. doi: 10.1007/s00410-009-0465-7

Rosera, J. M., Coleman, D. S., and Stein, H. J. (2013). Re−evaluating genetic models for porphyry Mo mineralization at Questa, New Mexico: implications for ore deposition following silicic ignimbrite eruption. *Geochem. Geophy. Geosyst.* 14, 787–805. doi: 10.1002/ggge.20048

Sakata, S., Hirakawa, S., Iwano, H., Danhara, T., Guillong, M., and Hirata, T. (2017). A new approach for constraining the magnitude of initial disequilibrium in Quaternary zircons by coupled uranium and thorium decay series dating. *Quat. Geochronol.* 38, 1–12. doi: 10.1016/j.quageo.2016.11.002

Schmitt, A. K., Stockli, D. F., Lindsay, J. M., Robertson, R., Lovera, O. M., and Kislitsyn, R. (2010). Episodic growth and homogenization of plutonic roots in arc volcanoes from combined U–Th and (U–Th)/He zircon dating. *Earth Planet. Sci. Lett.* 295, 91–103. doi: 10.1016/j.epsl.2010.03.028

Schoene, B., Schaltegger, U., Brack, P., Latkoczy, C., Stracke, A., and Gunther, D. (2012). Rates of magma differentiation and emplacement in a ballooning pluton recorded by U-Pb TIMS-TEA, Adamello batholith, Italy. *Earth Planet. Sci. Lett.* 355, 162–173. doi: 10.1016/j.epsl.2012.08.019

Shamloo, H. I., and Till, C. B. (2019). Decadal transition from quiescence to supereruption: petrologic investigation of the Lava Creek Tuff, Yellowstone Caldera, WY. *Contrib. Mineral. Petrol.* 174, 32.

Shane, P., Smith, V., and Nairn, I. (2003). Biotite composition as a tool for the identification of Quaternary tephra beds. *Quat. Res.* 59, 262–270. doi: 10.1016/s0033-5894(03)00012-7

Sláma, J., Kosler, J., Crowley, J. L., Gerdes, A., Hanchar, J., Horstwood, M., et al. (2007). Plesovice zircon - A new natural standard for U-Pb and Hf isotopic microanalysis. *Geochim. Cosmoch. Acta* 71, A947–A947.

Sliwinski, J. T., Bachmann, O., Dungan, M., Huber, C., Deering, C., Lipman, P., et al. (2017a). Rapid pre-eruptive thermal rejuvenation in a large silicic magma body: the case of the Masonic Park Tuff, Southern Rocky Mountain volcanic field, CO, USA. *Contrib. Mineral. Petrol.* 172:30.

Sliwinski, J. T., Ellis, B., Dávila-Harris, P., Wolff, J., Olin, P., and Bachmann, O. (2017b). The use of biotite trace element compositions for fingerprinting magma batches at Las Cañadas volcano. Tenerife. *Bull. Volcanol.* 79, 1.

Sliwinski, J. T., Guillong, M., Liebske, C., Dunkl, I., Von Quadt, A., and Bachmann, O. (2017c). Improved accuracy of LA-ICP-MS U-Pb ages of Cenozoic zircons by alpha dose correction. *Chem. Geol.* 472, 8–21. doi: 10.1016/j.chemgeo.2017.09.014

Sliwinski, J., Bachmann, O., Ellis, B., Dávila-Harris, P., Nelson, B., and Dufek, J. (2015). Eruption of shallow crystal cumulates during explosive phonolitic eruptions on Tenerife, Canary Islands. *J. Petrol.* 56, 2173–2194. doi: 10.1093/petrology/egv068

Smith, V. C., Pearce, N. J., Matthews, N. E., Westgate, J. A., Petraglia, M. D., Haslam, M., et al. (2011). Geochemical fingerprinting of the widespread Toba tephra using biotite compositions. *Quat. Int.* 246, 97–104. doi: 10.1016/j.quaint.2011.05.012

Streck, M. J. (2014). Evaluation of crystal mush extraction models to explain crystal-poor rhyolites. *J. Volcanol. Geother. Res.* 284, 79–94. doi: 10.1016/j.jvolgeores.2014.07.005

Szymanowski, D., Ellis, B. S., Wotzlaw, J.-F., and Bachmann, O. (2019). Maturation and rejuvenation of a silicic magma reservoir: high-resolution chronology of the Kneeling Nun Tuff. *Earth Planet. Sci. Lett.* 510, 103–115. doi: 10.1016/j.epsl.2019.01.007

Szymanowski, D., Wotzlaw, J.-F., Ellis, B. S., Bachmann, O., Guillong, M., and von Quadt, A. (2017). Protracted near-solidus storage and pre-eruptive rejuvenation of large magma reservoirs. *Nat. Geosci.* 10, 777–782. doi: 10.1038/ngeo3020

Tappa, M. J., Coleman, D. S., Mills, R. D., and Samperton, K. M. (2011). The plutonic record of a silicic ignimbrite from the Latir volcanic field, New Mexico. *Geochem. Geophys. Geosyst.* 12:Q10011.

Walker, B. A. Jr., Bergantz, G. W., Otamendi, J. E., Ducea, M. N., and Cristofolini, E. A. (2015). A MASH zone revealed: the mafic complex of the Sierra Valle Fértil. *J. Petrol.* 56, 1863–1896. doi: 10.1093/petrology/egv057

Watson, E., Wark, D., and Thomas, J. (2006). Crystallization thermometers for zircon and rutile. *Contrib. Mineral. Petrol.* 151:413. doi: 10.1007/s00410-006-0068-5

Watson, E. B. (1977). Partitioning of manganese between forsterite and silicate liquid. *Geochim. Cosmoch. Acta* 41, 1363–1374. doi: 10.1016/0016-7037(77)90079-5

Wiedenbeck, M., Alle, P., Corfu, F., Griffin, W. L., Meier, M., Oberli, F., et al. (1995). 3 Natural Zircon Standards for U-Th-Pb, Lu-Hf, trace-element and ree analyses. *Geostand. Newsletter* 19, 1–23. doi: 10.1111/j.1751-908x.1995.tb00147.x

Wilcock, J., Goff, F., Minarik, W. G., and Stix, J. (2012). Magmatic recharge during the formation and resurgence of the Valles Caldera, New Mexico, USA: evidence from quartz compositional zoning and geothermometry. *J. Petrol.* 54, 635–664. doi: 10.1093/petrology/egs078

Wilson, C., and Charlier, B. (2009). Rapid rates of magma generation at contemporaneous magma systems, Taupo Volcano, New Zealand: insights from U–Th model-age spectra in zircons. *J. Petrol.* 50, 875–907. doi: 10.1093/petrology/egp023

Wolff, J. A., Ellis, B., Ramos, F. C., Starkel, W. A., Boroughs, S., Olin, P. H., et al. (2015). Remelting of cumulates as a process for producing chemical zoning in silicic tuffs: a comparison of cool, wet and hot, dry rhyolitic magma systems. *Lithos* 236, 275–286. doi: 10.1016/j.lithos.2015.09.002

Wotzlaw, J. F., Bindeman, I. N., Watts, K. E., Schmitt, A. K., Caricchi, L., and Schaltegger, U. (2014). Linking rapid magma reservoir assembly and eruption trigger mechanisms at evolved Yellowstone-type supervolcanoes. *Geology* 42, 807–810. doi: 10.1130/g35979.1

Wotzlaw, J. F., Schaltegger, U., Frick, D. A., Dungan, M. A., Gerdes, A., and Gunther, D. (2013). Tracking the evolution of large-volume silicic magma reservoirs from assembly to supereruption. *Geology* 41, 867–870. doi: 10.1130/g34366.1

Conflict of Interest: The authors declare that the research was conducted in the absence of any commercial or financial relationships that could be construed as a potential conflict of interest.